High Fidelity Physics Simulation-Based Convolutional Neural Network for Automotive Radar Target Classification Using Micro-Doppler

USHEMADZORO CHIPENGO[ID], **ARIEN P. SLIGAR**[ID], **STEFANO MIHAI CANTA**[ID], **MARKUS GOLDGRUBER**, **HEN LEIBOVICH**[ID], AND **SHAWN CARPENTER**

Ansys Inc., Canonsburg, PA 15317, USA

Corresponding author: Ushemadzoro Chipengo (ushe.chipengo@ansys.com)

ABSTRACT Detection and classification of vulnerable road users (VRUs) such as pedestrians and cyclists is a key requirement for the realization of fully autonomous vehicles. Radar-based classification of VRUs can be achieved by exploiting differences in the micro-Doppler signatures associated with VRUs. Specifically, machine learning (ML) algorithms can be trained to classify VRUs using the spectral content of radar signals. The performance of these models depends on the quality and quantity of the data used during the training process. Currently, data collection is typically done through measurements or low fidelity physics, primitive-based simulations. The feasibility of carrying out measurements to collect training data is typically limited by the vast amounts of data required and practicality issues when using VRUs like animals. In this paper, we present a computationally efficient, high fidelity physics-based simulation workflow that can be used to obtain a large quantity of spectrograms from the micro-Doppler signatures of VRUs. The simulations are conducted on full-scale VRU models with a 77 GHz, frequency-modulated continuous-wave (FMCW) radar sensor model. Here, we collect the spectrograms of 4 targets; car, pedestrian, cyclist and dog at different speeds and angles-of-arrival. This data is then used to train a 5-layer convolutional neural network (CNN) that achieves nearly 100% classification accuracy after 5 epochs. Studies are conducted to investigate the impact of training data size, velocity and observation time window size on the accuracy of the CNN. Results from this study demonstrate how an accuracy of 95% can be realized using spectrograms obtained over a 0.2 s time window.

INDEX TERMS Automotive radar, micro-Doppler, machine learning, convolutional neural networks, FMCW, simulation.

I. INTRODUCTION

Autonomy and electrification have emerged as key drivers of innovation in the automotive industry in recent years. The ultimate goal of the autonomy initiative is the deployment of a fully autonomous (Level-5) vehicle that can safely drive itself in any conditions that a human driver can operate in. To achieve the autonomy goal, various advanced driver assistance systems (ADAS) have been developed to provide the vehicle with complete situational awareness. Light detection and ranging (Lidar), radio detection and ranging (radar), visible spectrum cameras and ultrasonic sensors are the main sensing technologies employed in ADAS [1]–[4]. Radar is

The associate editor coordinating the review of this manuscript and approving it for publication was Weimin Huang [ID].

a relatively cheaper (compared to Lidar) sensing technology that can be used to determine the range, velocity, and angle-of-arrival of multiple targets simultaneously in poor lighting conditions and inclement weather [5]. Various radar sensors centered around 77 GHz have been developed and tested recently for automotive applications [6]–[11].

Another motivating factor for the development of fully autonomous vehicles is the need to make roads safer. According to the NHTSA, 36,835 people lost their lives in road accidents in the U.S. in 2019 alone [12]. Research has shown that human error is responsible for 90% of all traffic accidents [13]. Collisions between vehicles and vulnerable road users (VRUs) such as pedestrians, cyclists and pets are common types of accident on public roads that can be fatal for the VRU or leave them severely injured [14]. Distraction on

the part of the driver or inattention of the VRU are the main causes of these types of accidents. Ideally, ADAS will eliminate this human error component by using sensors and systems that constantly detect potentially hazardous situations and respond faster than human beings. Fully autonomous vehicles will need to demonstrate a continuous and reliable ability to avoid collisions with VRUs before they are deemed safe for public roads. Crucial to this capability will be the ability to detect and classify VRUs.

Micro-Doppler has been identified as a possible means of classifying targets by analyzing the spectral content of reflected radar signals [15]. Using the Doppler effect, radar sensors can determine the velocity of targets. This velocity is typically associated with the bulk translation of the target. However, in addition to their bulk translation, non-rigid bodies can have further micro-motions such as rotation and vibration that can lead to Doppler frequency modulation [15], [16]. For example, the swinging arms and legs of humans are additional micro-motions that modulate the Doppler-induced frequency shift due to torso bulk translation. Human micro-Doppler has been investigated in [17]–[25]. The micro-Doppler response of cyclists was investigated in [14], [16], [26], [27]. In [28], [29], studies were conducted to measure the micro-Doppler response of drones and birds at 24 GHz and 94 GHz. Specifically, it was shown in [28] how the wing-beat of birds and the rotation of drone propeller blades leads to unique micro-Doppler signatures. Micro-Doppler was also used to classify vehicle types when considering tracked and wheeled vehicles [30].

Convolutional neural networks (CNNs) are deep-learning (DL) algorithms capable of conducting image classification. CNNs have been used for micro-Doppler based VRU classification. Specifically, CNNs can be trained to classify VRUs using spectrograms (images of the time-frequency representation of the radar signals) [21], [22], [29], [32], [35]–[39]. The classification accuracy of a CNN depends on the quality, labeling and quantity of the data used to train it. For micro-Doppler based VRU classification, this means that a small training data sample, poorly labeled data or noisy data can lead to overfitting. Traditionally, spectrograms have been obtained using direct measurement [16], [17], [19], [21], [23], [25], [31], [32], [38] and primitive-based simulations [14], [16], [22], [24], [26], [27], [29], [32], [35], [37]. Measurements are valuable, however, CNNs typically require thousands of data samples for reliable training. Collecting such massive data sets can be expensive, time consuming and impractical in some cases.

Primitive-based simulations have been conducted to rapidly obtain massive data sets that can be accurately labeled. Historically, the primitive-based simulation approach has been used because it is computationally inexpensive when compared to full-wave electromagnetic simulations [42]. Primitive-based simulations represent distributed targets as a series of geometrical primitives or points. For example, the human body can be decomposed into 16 parts with time varying motion [20], [41]. Kinematics

are introduced using video motion capture (MOCAP) data [43], [44], [47], [49], [50], [52]–[56] or kinematic models [40], [50]. The analytical equations used in primitive-based simulations make far-field assumptions and other radar cross section (RCS) approximations that reduce the accuracy of this approach for automotive radar applications which are inherently in the near field [53]. This approach does not also account for shadowing or multi-path wave propagation [54]. Furthermore, the primitive-based simulation approach cannot be easily extended to complex, arbitrary targets like animals, cyclists and cars. In [26], [57], cyclists were represented by a multi-target reflection point model while a skeleton version of a horse was used in [43].

In this paper, we present a high-fidelity, physics-based shooting and bouncing ray (SBR) simulation approach that can be used to obtain accurate spectrograms from full scale representations of VRUs and vehicles [58]–[64]. Here we use a synthetic, frequency-modulated continuous-wave (FMCW) 77 GHz radar sensor to obtain over 4,500 spectrograms of four targets; pedestrian, dog, cyclist and car. Fig.1 shows the pedestrian, cyclist, dog and car models used in this simulation study along with measurement setups from [16], [25], [28], [48] and primitive based-models used in [22], [26], [47], [52]. We conduct studies to demonstrate variations of VRU spectrograms as the angle-of-arrival changes. Furthermore, we demonstrate the variation in spectrograms across the target classes. A 5-layer CNN is then trained using the collected spectrograms and is shown to demonstrate nearly 100% accuracy after just 5 epochs. Robustness studies are also conducted to study the impact of data set size, velocity and time observation window on the classification accuracy of the model. Results from this study demonstrate how a classification accuracy of 95% can be realized using spectrograms obtained over a 0.2 s observation window.

This paper is organized as follows: section II focuses on the various techniques used to obtain micro-Doppler data. section III focuses on micro-Doppler theory, validation of simulation workflow and the post processing conducted on the results. In section IV, we present the micro-Doppler response of individual targets and how they vary as their angle-of-arrival changes. Section V focuses on the CNN training and testing. Here, various data set sizes and time observation windows are used to test the CNN model robustness. A discussion on measurement and simulation data for machine learning applications then follows in section VI.

This paper has two main contributions. First, we present a comprehensive, large-scale, spectrogram-based classification study of four representatives from the classes of mobile targets typically encountered on roads. Most previous works have only focused on combinations of two target classes (e.g., pedestrian and vehicle) or intra-class activity classification (e.g., human activity classification). To the best of the authors' knowledge, this comprehensive study is the first of its kind for simulation based approaches. Second, we propose a high-fidelity, physics-based simulation approach that can be used as an optimum compromise between
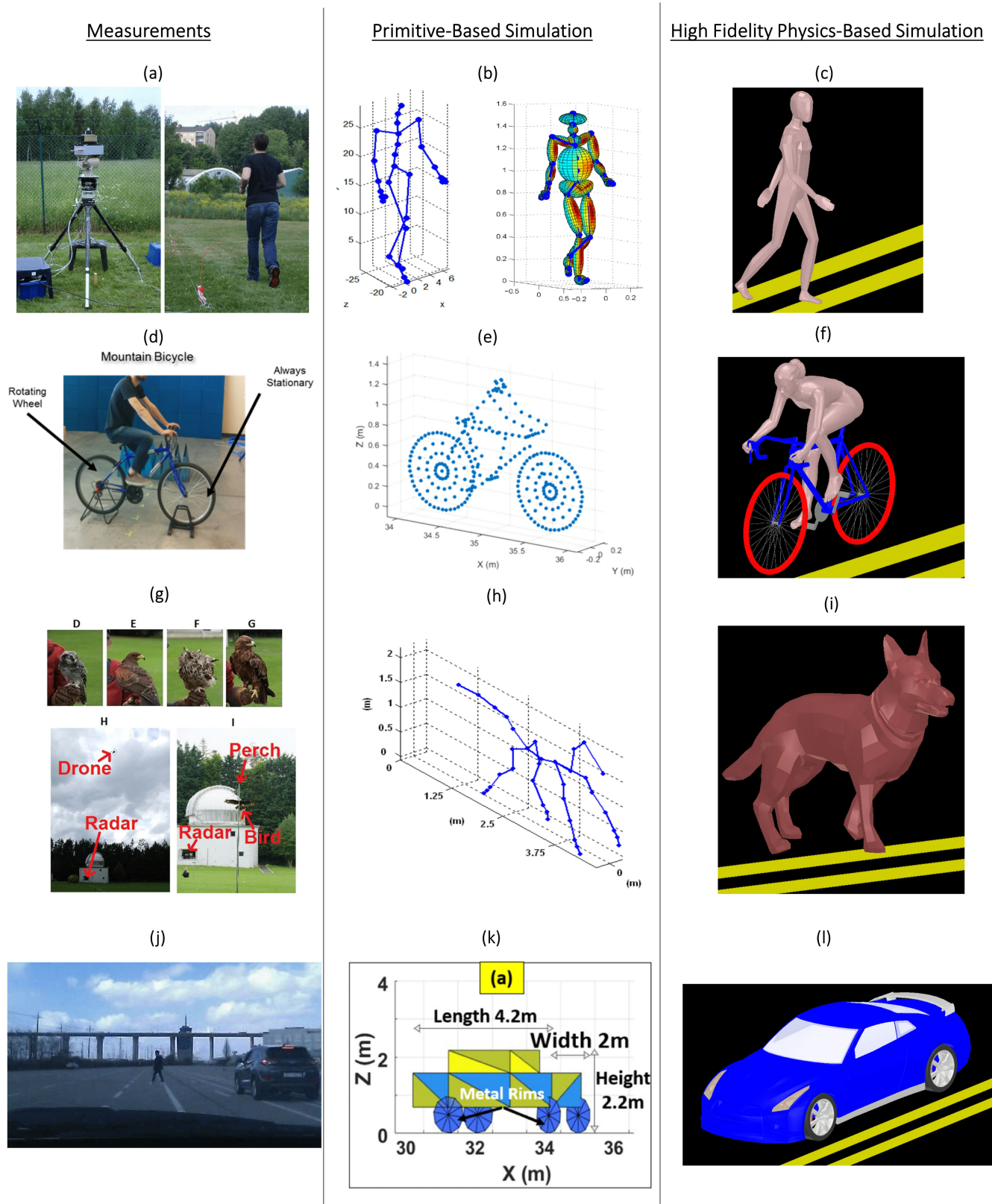
FIGURE 1. Methods used to obtain spectrograms for convolutional neural network (CNN) training. Measurement: (a) [25], (d) [16], (g) [28], (j) [48]. Primitive-based simulation:(b) [22], (e) [79], (h) [52], (k) [47]. High fidelity physics-based simulation (this work): (c), (f), (i) & (l).

primitive-based simulations and measurement. Specifically, our proposed simulation approach is more accurate than primitive-based simulations while being significantly faster, cheaper and more practical to conduct than measurements. High-fidelity, physics-based simulation data can be used for measurement data augmentation or as a starting point for training CNN-based VRU classifiers that may prevent future accidents and ultimately save lives.

II. MICRO-DOPPLER DETERMINATION METHODS FOR CNN TRAINING

The classification accuracy of a convolutional neural network greatly depends on the quality of data used to train it. Specifically, CNNs usually require large quantities of accurate and well labeled data to achieve better generalization for new data classification. These constraints on the data quantity, quality and labeling mandate a balancing act between cost, speed, practicality, repeatability and accuracy of the methods used to generate the CNN training data. In this section, we discuss the two currently used micro-Doppler data generation techniques and then propose a high-fidelity, shooting and bouncing ray solver approach.

A. MEASUREMENT

Various campaigns have been undertaken to measure micro-Doppler characteristics via direct measurement [16], [17], [19], [21], [23], [25], [31], [32], [38]. A 94 GHz radar was used for measurements in [23] to obtain spectrograms for human motion detection. The micro-Doppler responses of pedestrians and cyclists were measured at 77 GHz in [16]. In [47] micro-Doppler spectrograms of a pedestrian, bicycle and car were measured while following defined trajectories using a 7.5 GHz radar. Micro-Doppler measurements have also been conducted on animal subjects. Recently, the micro-Doppler characteristics of four species of birds and three drone types were measured using 24 GHz and 94 GHz radar sensors in [28]. Most of the mentioned measurement campaigns yielded accurate spectrograms in very small quantities, thus making the data volume obtained unsuitable for reliable machine learning (ML) applications. Efforts have been undertaken to obtain larger quantities of radar data for ML-based applications. A 77 GHz FMCW radar sensor was used in [48] to obtain 2000 samples of measured data for developing a feature-based support vector machine (SVM) human-vehicle classifier. However, the dependence of this classifier on the radar cross section (RCS) of the targets can make it unreliable in complex environments that have multiple, high RCS targets. A passive WiFi radar (PWR) measurement campaign was conducted in [44] to obtain micro-Doppler signatures of humans carrying out various activities for healthcare monitoring. The spectrograms from these measurements were used to train a convolutional neural network with high levels of classification accuracy. However, these measurements were conducted in a very controlled indoor environment, free from noise, clutter and large RCS targets encountered on roads.

Measurements are valuable because they can provide highly accurate results that include all the practically encountered effects such as noise, clutter, sensor sensitivity limitations, interference and complex multipath effects. However, measurements can be expensive, time consuming and impractical or dangerous in some cases. To produce large quantities of unique data from moving subjects requires high degrees of control and repeatability. While it can be hard for a human to repeat thousands of exact movements with precision, it is nearly impossible to train an animal to do so. Consistent and accurate data labeling are also challenging when conducting measurements. It is also difficult to create and sustain an interference free environment for accurate outdoor, open road measurements at 77 GHz. It may be difficult to train a CNN using highly noisy data. For this reason, RCS measurements on cars, cyclists and pedestrians are usually conducted in well controlled indoor chambers in [42], [51]. Therefore, the speed, cost, practicality and repeatability limitations of measurements can make them unattractive for initial CNN training.

B. PRIMITIVE-BASED SIMULATIONS

To address the challenges posed by measurements, primitive-based simulation methods have been used as a means to rapidly obtain large quantities of accurately labeled spectrograms for ML-based target classification [14], [16], [22], [24], [26], [27], [29], [32], [35], [37]. Primitive-based simulation methods obtain the micro-Doppler signatures of targets by decomposing the targets into independent points or primitive shapes. In this approach, the total radar returns of a target are viewed as the summation of the complex, time-varying responses of its constitutive primitives [50], [52], [53]. The RCS of each primitive is calculated using a well-defined analytical formula and is applied to the radar-range equation to determine the radar-return signal [50], [53].

In [46], three-dimensional models of a car, bicycle, rickshaw and truck were decomposed into triangular facet primitives and used to simulate ISAR images for automotive radar. Here, each triangular facet was considered to be an independent scatterer. When using the primitive-based approach, the human body is usually represented by a series of ellipsoids (see Fig.1). The position and velocity of each primitive is obtained from kinematic models or motion-capture (MOCAP) data. The popular Boulic *et al.* [40] walking model has been extensively used to describe the walking human gait cycle. A key disadvantage of this kinematic model is that it only describes human walking activities. Video motion-capture technology addresses these challenges by providing a platform for capturing arbitrary human activities while providing more realistic kinematics [43], [44], [47], [49], [50], [52]–[56]. The Carnegie Mellon University (CMU) Motion Research Laboratory human activity MOCAP database is a widely used resource for primitive-based micro-Doppler simulation [56]. Recent works have used Microsoft's Kinect system as a cheaper,
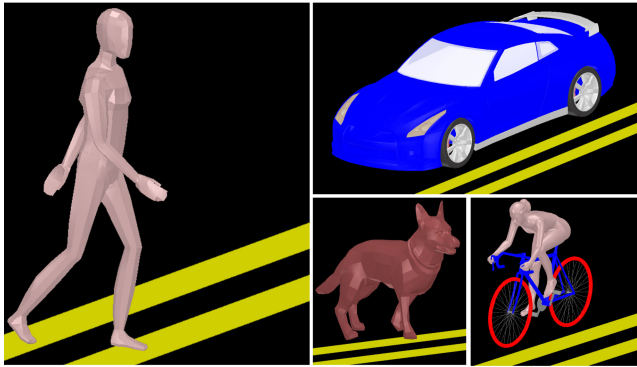
FIGURE 2. Full-scale, 3-dimensional CAD models representing 'actors' used in HFSS SBR+ to obtain Doppler information for spectrogram analysis. A CNN will be trained to classify VRUs using spectrograms from a pedestrian, car, dog and cyclist.

FIGURE 3. Setup for validating the simulation workflow and the post processing technique used in this work. The plate at the center represents the bulk translation while the spheres represent additional rotational micro-motion.

FIGURE 4. Spectrogram obtained from simulation setup in Fig.3. The central line belongs to the steel plate while the sinusoidal curves belong to the two spheres.

marker-less system for recording human activity kinematics [49]. A limitation of MOCAP is that it cannot be reliably used on animals, cyclists or vehicles [43]. Furthermore, it would be difficult to dictate the motion of an animal subject in a precise manner for a micro-Doppler measurement campaign.

Regardless of the source or fidelity of the kinematics data, primitive-based simulations are based on far-field approximations [39], [43], [46], [47], [49], [50], [53]. The radar-range formulation inherently assumes that targets are in the far-field. At high frequencies such as 77 GHz, the far field region is several kilometers away, well beyond the range of automotive radar [51], [65]. This means all of the relevant VRUs are in the near field of the radar sensor. It was demonstrated in [68] that the RCS of vehicles is range-dependent in the near field and drastically changes from ranges of 5 m to 50 m. The primitive-based simulation approach does not also explicitly simulate wave propagation. Because of this, it cannot account for second order effects such as multipath propagation and shadowing between primitives [54]. This means that the accuracy of this approach will diminish as the radar scene geometrical complexity increases. Using a similar approach, it was also assumed in [46] that all scatterers are visible to the radar, thus neglecting shadowing and multipath effects. As the complexity of targets under investigation increases, it can become harder to decompose targets like cyclists, road infrastructure, animals or vehicles into primitives. Fig.1 shows low-fidelity, primitive/point-based models of a cyclist, pedestrian, vehicle and horse used for micro-Doppler simulations. A series of point sized reflectors was used in [43] to represent the road.

C. RAY TRACING SIMULATIONS

The primitive-based simulation workflow was developed to address the challenges associated with simulating electrically large problems at high frequencies with full-wave electromagnetic solvers. Specifically, at 77 GHz, the wavelength is approximately 3.9mm. Therefore, a full-scale traffic scene can be billions of cubic wavelengths in size. Physics-based, asymptotic, ray-tracing electromagnetic solvers address the high computational demand issues of full-wave methods
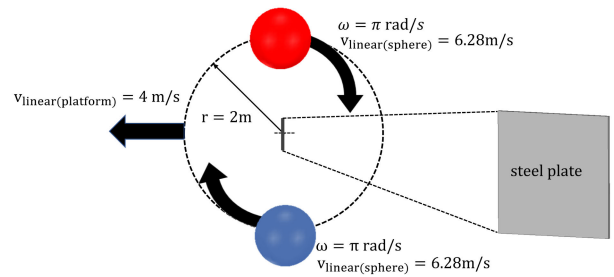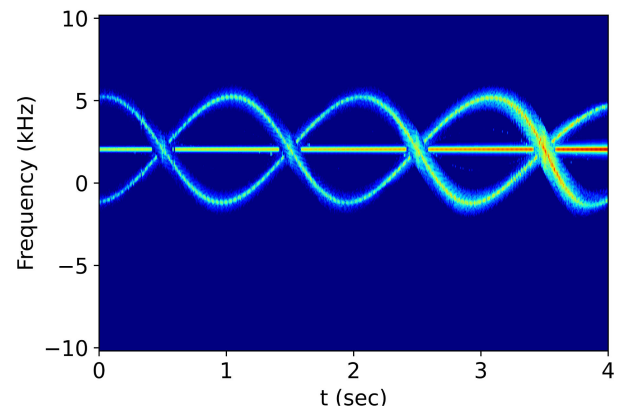
while retaining high accuracy for electrically large problems [65]–[67]. A shooting and bouncing ray solver was used in [54] to obtain the radar cross section of a human engaged in a series of dynamic motions. In this paper, we use Ansys' High Frequency Structure Simulator (HFSS) Shooting and Bouncing Rays (SBR+) solver [59], [61]–[64].

HFSS SBR+ is a hybridization of geometrical optics (GO) and physical optics (PO). Here, multiple GO rays are launched from the transmitting antenna and vector-field weighted by the true antenna radiation pattern (see Fig. 5). These GO rays then 'paint' PO currents on the scattering CAD geometry (in this case the radar scene and its actors). The PO currents are then re-radiated and are considered as the scattered field. GO is used again to create a new set of reflected rays from the first hit points and the process goes on and on. In this way, HFSS SBR+ uses GO to extend PO to multiple bounces. In this work, we used 5 bounces. HFSS SBR+ also applies physical theory of diffraction (PTD) wedge correction and creeping waves (CW) to account for the distortion of surface currents near discontinuities and curvatures. Uniform theory of diffraction (UTD) is used to augment GO rays thus allowing illumination of CAD faces in the shadow region of the transmitter according to GO [67]. Since this approach does not require a target to be decomposed into primitives, this simulation workflow can be used
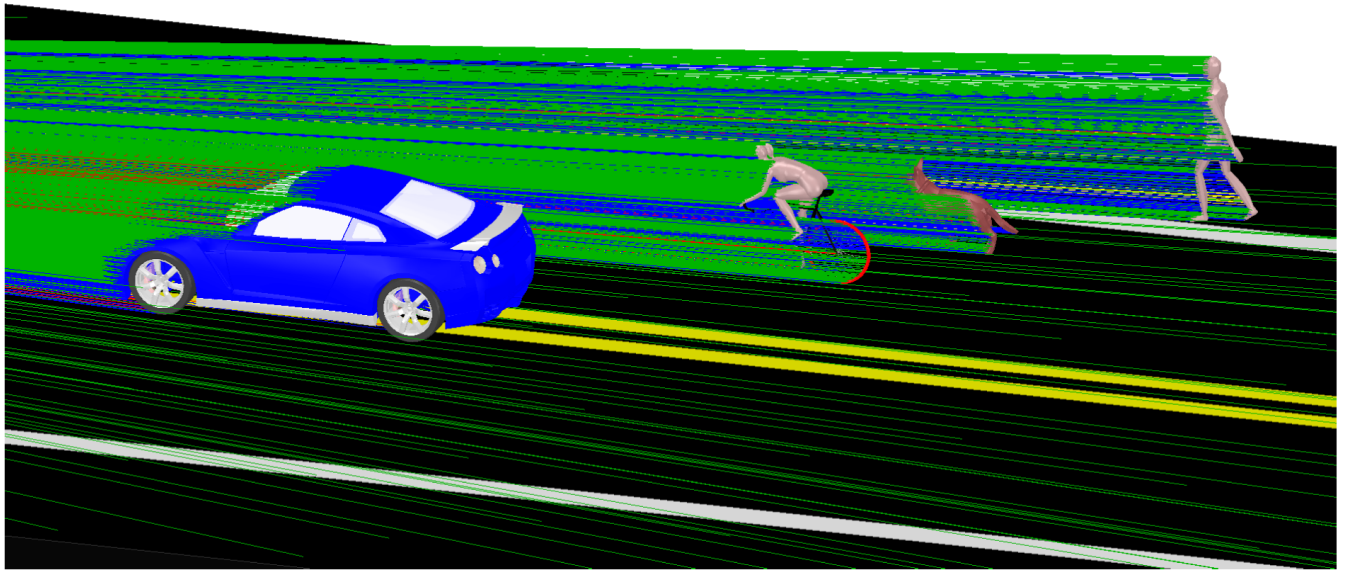
FIGURE 5. Geometrical Optics-based (GO) visual ray tracing of full-scale, 3-dimensional CAD objects ('actors') used in HFSS SBR+ to obtain spectrograms. Each of the lines incident on the CAD represents a GO ray track. A CNN will be trained to classify VRUs using spectrograms from a pedestrian, car, dog and cyclist.

on any arbitrarily shaped targets as shown in Fig.2. The approach used here means that we are appropriately treating automotive radar as a near field problem. The SBR+ approach considers the transmission, reflection, diffraction, refraction and multi-path physics of electromagnetic wave propagation. With this framework, the SBR+ solver can also be used in installed antenna performance studies [61], antenna-to-antenna coupling and for determining RCS of electrically large targets [63]. Therefore, the physics-based ray-tracing solver approach used in this work provides an optimum balance between the measurement method and the primitive-based simulation approach when trying to obtain large quantities of spectrograms.

III. MICRO-DOPPLER THEORY AND SIMULATION WORKFLOW VALIDATION
A. MICRO-DOPPLER THEORY
Radar is a sensing technology that can be used to determine the range, velocity and angle-of-arrival of multiple targets simultaneously. The range of a target can be determined by measuring the round-trip, time-of-flight of a transmitted signal and its reflected echo [69]. Angle of arrival can be obtained by determining the progressive phase shift of a signal arriving at an antenna array whose elements have a known physical spacing [70]–[73]. Velocity is determined by exploiting the Doppler-effect. Specifically, a target with a velocity v relative to a stationary transmitter will induce a frequency shift, f_d in the reflected signal given by [19]

$$f_\mathrm{d} = F_t \frac{2v}{c} cos\theta cos\phi \qquad (1)$$

Here F_t, θ, ϕ and c are the frequency of the transmitted signal, angle-of-arrival in the elevation plane, angle-of-arrival in the azimuthal plane and the speed of light, respectively.

For a point scatterer, the Doppler frequency shift is characterized by a single frequency.

Non-rigid bodies can have micro-motions such as rotation or vibrations in addition to their bulk translation. Such micro-motions introduce frequency modulation on the radar signal. This additional frequency modulation of the reflected signal due to micro-motions on non-rigid bodies is called the micro-Doppler effect [15], [16], [19]. In order to exploit convolutional neural networks for VRU classification, the embedded micro-Doppler information in the radar signal needs to be presented in a format that CNNs can use. To do this, micro-Doppler information is presented in the form of a spectrogram, a slow time-frequency (TF) representation of the signal [21], [22], [29], [32], [37], [39]. The Short-Time Fourier Transform (STFT) is an efficient way of conducting TF analysis. The STFT approach involves conducting a Fourier transform over a small time window (coherent processing interval (CPI) in the case of FMCW radar) and then sliding the window in time [19], [20]. The continuous STFT, $X(\tau, f)$ of $x(t)$ is given by

$$STFT\{x(t)\}(\tau, f) \equiv X(\tau, f) = \int_{-\infty}^{\infty} x(t)w(t - \tau)e^{-j2\pi ft}dt \qquad (2)$$

Here $w(t)$ is the window function and f is frequency. The spectrogram in decibels is given by

$$spectrogram(\tau, f) = 10log_{10} \mid X(\tau, f) \mid^2 \qquad (3)$$

B. SIMULATION WORKFLOW AND POST PROCESSING VALIDATION
The synthetic radar returns used to obtain spectrograms in this study were obtained using HFSS SBR+. Here, HFSS SBR+ was used to create a virtual FMCW radar. A key advantage

TABLE 1. Radar parameters for simulation setup.

Parameter	Value
Center Frequency	76.5 GHz
Start Frequency	76.3 GHz
Stop Frequency	76.7 GHz
Bandwidth	400 MHz
Maximum Range	75m
Range Resolution	0.375m
Number of gated range bins	200
Velocity Period	60 m/s
Velocity Resolution	0.1172 m/s
Pulse Repetition Frequency (PRF)	30.624 KHz
Coherent Processing Interval	16.719 ms
Number of pulses	512

of this workflow is that it gives flexibility in designing the FMCW waveform. Specifically, it is possible to investigate many different waveforms and how they can impact classification. This is something that would be challenging to do in measurements. Furthermore, simulation makes it possible to collect data for any number of different waveforms or radar sensors on the same scenarios. Such a capability can aid in deciding the waveform or sensor required for target classification applications. Table 1 shows the radar performance parameters and the associated FMCW waveform parameters used in this study.

For a single-channel radar FMCW sensor, each CPI provides a 2-dimensional radar data matrix. The first dimension is along the frequency samples in each chirp while the second dimension spans samples of a single frequency from chirp to chirp. A single range-Doppler map can be obtained by conducting a 2-dimensional fast Fourier transform (FFT) on this matrix [62]. However, the 2D FFT analysis can be reduced to a 1D FFT analysis since spectrograms only require the frequency content of the signal per CPI [20]. Specifically, for each CPI, the Doppler information was extracted by conducting an FFT on samples of a single frequency (range bin) obtained over all the pulses in the CPI.

To validate the simulation workflow used here, two rotating steel spheres were placed around a steel plate. The steel plate had a linear velocity of 4 m/s while the spheres rotated at an angular velocity of π radians. At a radius r of 2 m, this angular velocity translates to maximum linear velocities of $\omega r = \pm 6.28$ m/s. Fig. 3 shows the simulation setup. The steel plate represents bulk translation motion while the spheres represent rotational micro-motion. The spectrogram should show 3 distinct spectrum tracks belonging to the plate and two spheres. From (1), the rotation of the spheres can be represented by a variation in θ, the elevation angle. Therefore, the spectrogram must show a straight line belonging to the plate and two sinusoidal curves offset by π radians phase shift. The maximum and minimum velocities of the spheres, relative to a stationary radar sensor are

$$v_{\text{linear(sphere)max}} = v_{\text{linear(platform)}} + v_{\text{linear(sphere)}}$$
$$= 4 \, \text{m/s} + 6.28 \, \text{m/s} = 10.28 \, m/s \quad (4)$$

$$v_{\text{linear(sphere)min}} = v_{\text{linear(platform)}} - v_{\text{linear(sphere)}}$$
$$= 4 \, \text{m/s} - 6.28 \, \text{m/s} = -2.28 \, \text{m/s} \quad (5)$$

Using (1), the linear velocity of the steel plate (bulk platform) of 4 m/s corresponds to a Doppler frequency shift, f_d of 2.040 kHz for transmission frequency of 76.5 GHz. For the spheres, their maximum and minimum velocities, 10.28 m/s and -2.28 m/s correspond to Doppler frequency shifts of 5.243 kHz and -1.163 kHz, respectively. Fig. 4 shows the spectrogram obtained from the simulation setup shown in Fig. 3. As expected, two sinusoidal curves belonging to the rotating spheres with maxima and minima at 5.243 kHz and -1.163 kHz, respectively are observed. A single track corresponding to the steel plate is shown at 2.040 kHz. The spectrogram was obtained using the discrete form of the STFT shown in (2). Specifically, a discrete Fourier transform was conducted on samples of a single frequency point across all the pulses in a single CPI. A moving time-window of 0.01 s was then used.

IV. MICRO-DOPPLER RESPONSE OF TYPICAL ROAD USERS

A pedestrian, four-legged animal, cyclist and car represent a large portion of moving target classes that a typical autonomous vehicle will encounter on the road. Here we use a dog as an ideal four-legged animal representative due to its high adoption rate as a pet. The ultimate goal for fully autonomous vehicles would not only be the ability to detect each of these targets but to classify them as well. Building upon correct classification, the next goal would be predictive intention recognition [14]. By predicting the possible future trajectory of a target, an autonomous vehicle can anticipate the engagement of specific maneuvers to prevent an accident. For example, an animal is more likely to perform random, unpredictable movements. This means that an autonomous vehicle in its vicinity would need to slow down in anticipation of sudden movements in any direction. In this section, we conduct a study of the micro-Doppler responses of a pedestrian, dog, cyclist and car. Specifically, HFSS SBR+ was used to obtain the synthetic radar returns from full scale, 3-dimensional models of each of these targets (see Fig.2) observed over a total time of 2 s. Table 2 shows the number of facets for each target.

The actors were animated using a coordinate system-based approach. Each actor had an anchor coordinate-system responsible for the bulk translational velocity. Rotation and oscillation coordinate systems were appropriately placed to introduce velocity-dependent micro-motions. Fig. 7 shows the actors and their associated coordinate systems used for animation. The cyclist motion is described using one anchor CS and seven rotation CS. The coordinate systems on the wheels and pedals were used as references for wheel and pedal rotation. The cycling motion of the cyclist was introduced through x, y, z translations and sinusoidal oscillations of the hips and legs using four coordinate systems. The human and dog micro-motion was introduced through sinusoidal-based oscillations of the limbs. Phase offsets were also introduced for each limb for a more accurate representation. The car wheel rotation used two coordinate systems
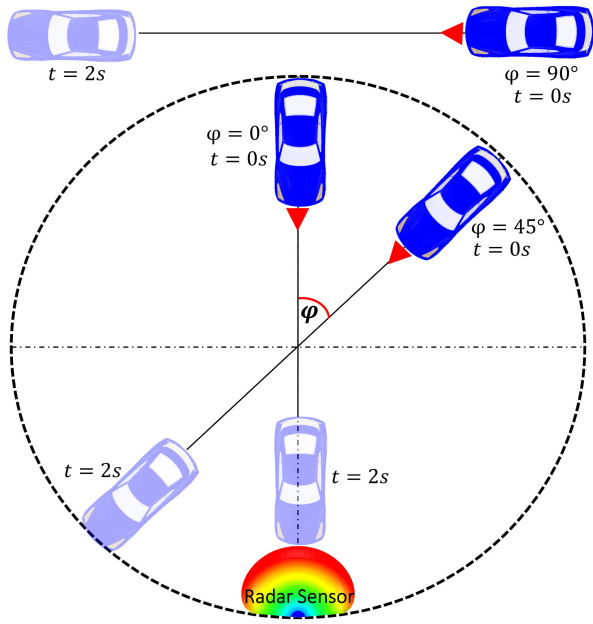
FIGURE 6. Simulation setup for obtaining the spectrograms of the actors shown in Fig.2. A spectrogram was obtained for each target at 3 key angles of arrival, $\phi = 0°$, $\phi = 45°$ and $\phi = 90°$.

FIGURE 7. Coordinate system (CS)-based animation for micro-Doppler simulation in HFSS SBR+. Each of the actors has a single anchor CS for the bulk translational motion. Micro-Doppler is introduced through rotation or oscillation at the rotation CS.

centrally located at the front and back of the car. The symmetric sinusoidal oscillations of the pedestrian, dog and cyclist limbs are approximations of the true kinematics. This is a limitation of the CS-based animation method used here. However, the animations look realistic enough upon inspection for initial classification studies. Future efforts will be aimed at integrating more realistic motions such as the ones from MOCAP or 3D animations with the HFSS SBR+ solver for increased fidelity.

The unique bulk velocities, rotation frequencies and oscillation frequencies for each actor were all tied to a single global time variable. Assuming a radar frame-rate of n fps, a parametric sweep was run to advance the simulation in time, $t = 1/n$. HFSS SBR+ then used the Accelerated Doppler Processing® feature to simulate a single CPI while accounting for target velocity and motion within each CPI. Assuming a frame rate of 30 fps over a 2 s time window, 61 CPIs were simulated to obtain a single spectrogram. Using a 6 core, Intel® Core(TM) i7 at 2.6GHz CPU, it approximately took 90s to obtain a single spectrogram.

Simulations were conducted in HFSS SBR+ to compare with results from measurements independently conducted by other authors in their works [16], [47], [78]. Specifically, we used measurement setup details from [16], [47], [78] to recreate the setups used in these works as shown in Fig. 8. While the simulation setups were not exact replicas of the measurement setups, our goal was to demonstrate similarity in the measured and simulated results to validate the fidelity of our simulation workflow. Fig. 8 shows 3 measurement setups and their corresponding simulation setups along with both measured and simulated spectrograms. Specifically,
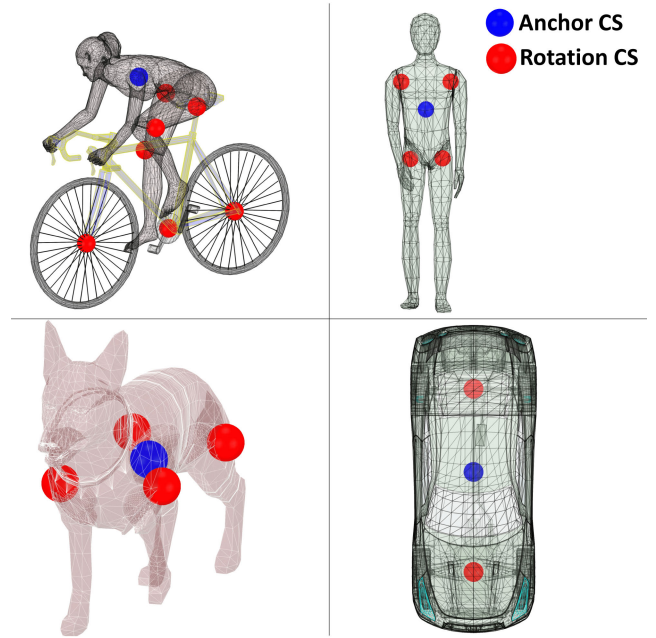
in [47], a car was driven towards a radar sensor for 15 m before executing a sharp turn 5 m away from the radar. The spectrogram obtained from measurements shows the characteristic micro-Doppler spread that occurs when the car turns and exposes its wheels. Similar behavior was observed in our simulations as shown in Fig. 8. The micro-Doppler of a cyclist was measured at 77 GHz in [16]. This setup was also virtually recreated in HFSS SBR+ for comparison. Fig. 8 shows good levels of agreement between the measured and simulated spectrograms. Both spectrograms show the sinusoidal-like micro-Doppler induced by the pedaling legs. Finally, the micro-Doppler of a stand-alone bicycle wheel was simulated for comparison with measured results from [78]. Here, a rotating bicycle wheel was placed in front of a radar sensor. The simulated spectrogram also showed good levels of agreement with the measured spectrogram. Here, a micro-Doppler induced Doppler spread due to the rotating tire treads and spokes was observed.

Similar simulations were conducted in [79]–[81] using the primitive-based simulation method. Specifically, a multi-point model of a bicyclist was simulated in [79]. Here, the bicyclist and the bicycle were represented by more than 144 scatter points as shown in Fig. 1(e). The model used here ignored internal occlusions within the bicyclist and used the same approach described in section II to obtain the total radar returns. The simulated spectrogram is shown in Fig. 9. This should be compared to the results shown in Fig. 8. Another primitive-based simulation was conducted in [43]. Here, a car was approximated by a single point scatterer. The simulated spectrogram is shown in Fig. 9 and should be compared to the results shown in Fig. 8. While the single-point
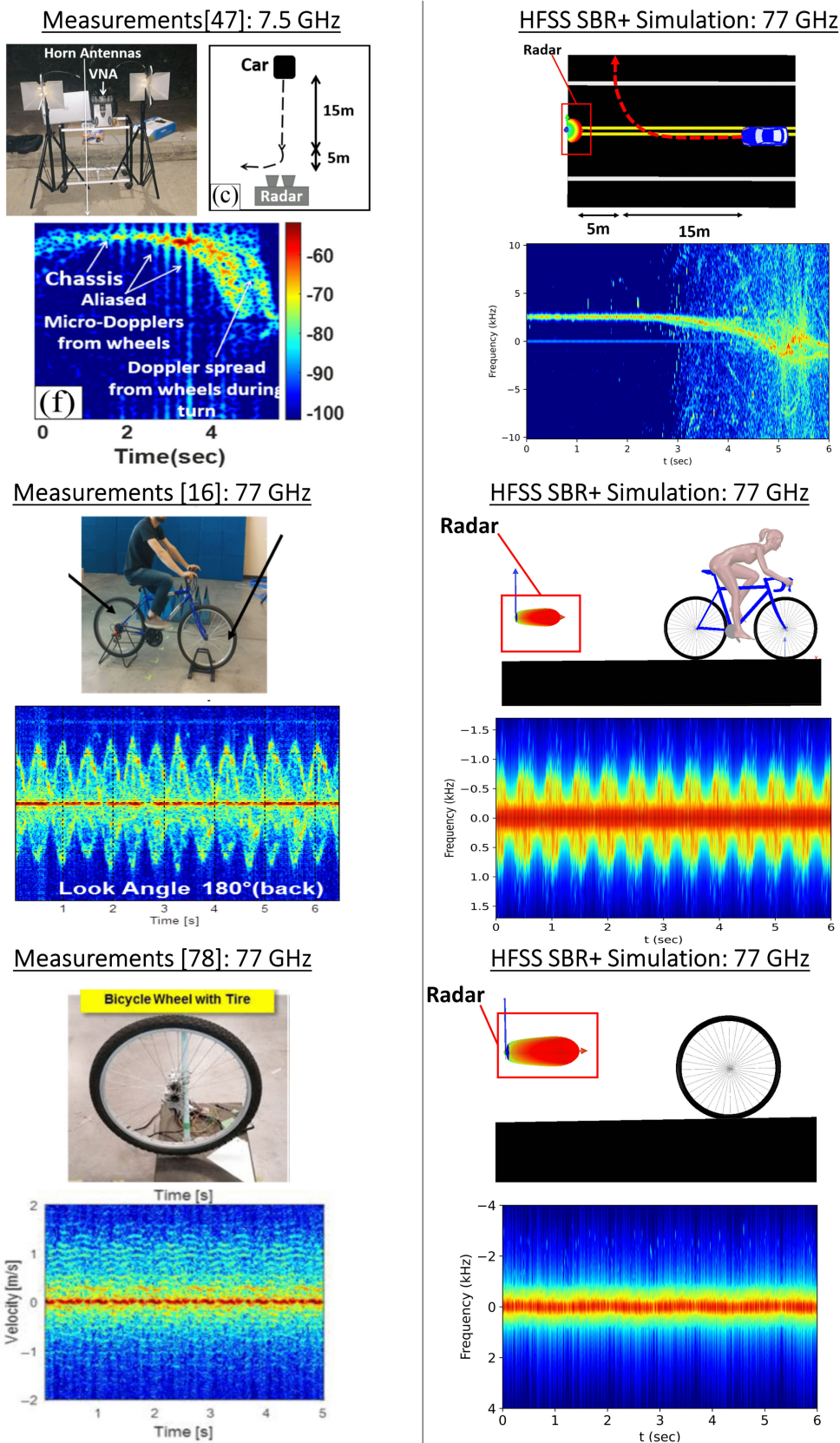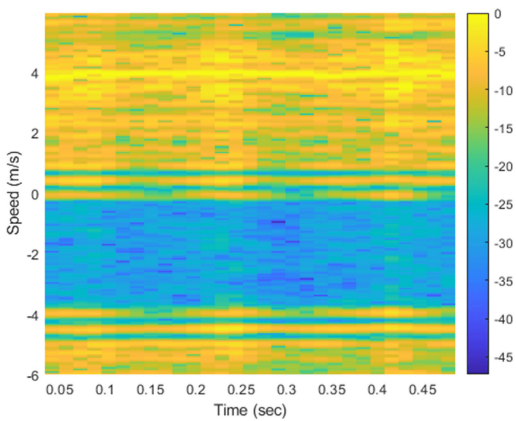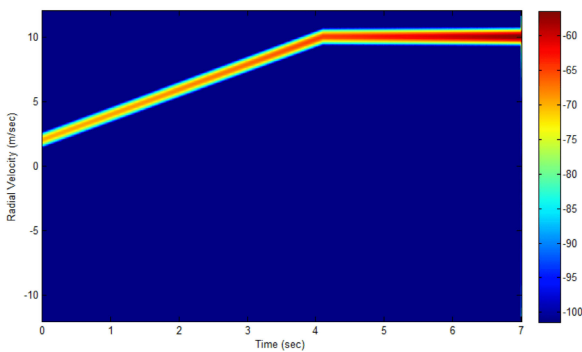
FIGURE 8. Measurement and simulation results from similar setups conducted at 7.5 GHz and 77 GHz, respectively. The measurements were conducted in [16], [47], [78] while the simulations are from this work.

Multi Point(>144) Bicyclist Model [79]

Single Point Car Model [43]

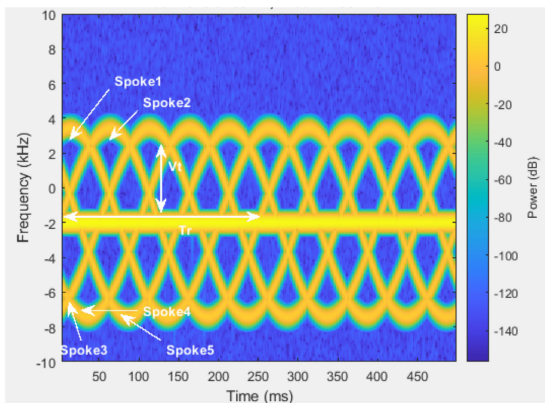## Six Point Car Wheel Model [80]

FIGURE 9. Micro-Doppler responses of a bicyclist [79], car [43] and car wheel with 5 spokes [80] using primitive-based simulations. The bicyclist is represented by over 144 points while the car is approximated by a single point scatterer.

scatterer approximation is valid for a car moving directly towards the radar sensor, it cannot capture any wheel-induced micro-Doppler effects. A similar approach was used in [57] with similar results. Finally, the micro-Doppler of a single car wheel was simulated in [80] using a 6-point scatterer model. Here, the wheel was assumed to have 5 spokes. The spokes were represented by 5 point scatterers rotating around a single point scatterer. The spectrogram from this simulation is shown in Fig. 9 and should be compared to results from Fig. 8. Results from [80] show the spectrogram of a wheel

TABLE 2. Description of Actors in Radar Scene.

Actor	Number of Facets
Car	21672
Pedestrian	2058
Dog	10150
Cyclist	22702

as a set overlapping discrete sinusoidal profiles due to the point-scatterer approximation.

Past works have shown how the primitive-based simulation approach can be used to obtain accurate spectrograms of human subjects when used in conjunction with motion capture data [22]. However, a comparison of Fig. 8 and Fig. 9 shows the accuracy limitations of the primitive-based simulation approach when considering complex targets such as bicyclists and cars. Specifically, the single-point representation of car is not an accurate model for obtaining the micro-Doppler of a vehicle at any angle of arrival (AoA) other than $\phi = 0°$ (see Fig. 6). On the other hand, a wheel is a distributed scatterer that cannot be accurately modeled by a set of discrete points as shown in Fig. 9. Such accuracy limitations may make primitive-based simulation approaches unreliable for obtaining micro-Doppler data for machine learning-based classification of complex targets such as cars and bicyclists.

A. SIMULATING DEPENDENCE OF SPECTROGRAMS ON AoA AND VRU ORIENTATION

To demonstrate the impact of the angles-of-arrival (AoA) and orientation on the spectrograms, a spectrogram was obtained for each target at 3 distinct AoA ($\phi = 0°$, $\phi = 45°$ and $\phi = 90°$) as shown in Fig.6. While the data in this section was obtained over 3 angles, the spectrograms for the overall CNN training were obtained for 180 distinct AoA spanning from $\phi = 0°$ to $\phi = 180°$.

B. PEDESTRIAN

A walking pedestrian can be considered as a target with a bulk translation attributed to its torso. The oscillatory micro-motions of the swinging arms and legs are responsible for the micro-Doppler. Fig. 10 shows the spectrograms of a pedestrian walking at a speed of 1.4 m/s observed over a 2 s time window. The spectrogram is described by a straight line and two sinusoidal profiles that are 180° out of phase. At $\phi = 0°$, the spectrogram of a pedestrian has similarities to the one shown in Fig. 4. However, the spectrogram of Fig. 4 has sinusoidal lines while the spectrogram shown in Fig. 10 has sinusoidal profiles whose area under the curve is completely filled in. This is because the simulation conducted with a full-scale pedestrian model accounts for the distributed nature of the pedestrian. On the other hand, the spheres used in Fig. 3 to obtain the spectrogram in Fig. 4 behave like point sources with less spatial distribution. The symmetrical and sinusoidal profiles obtained in the spectrograms for pedestrians in this work are artifacts of the sinusoidal kinematics approximation that was used here and not the actual HFSS SBR+ solver accuracy.
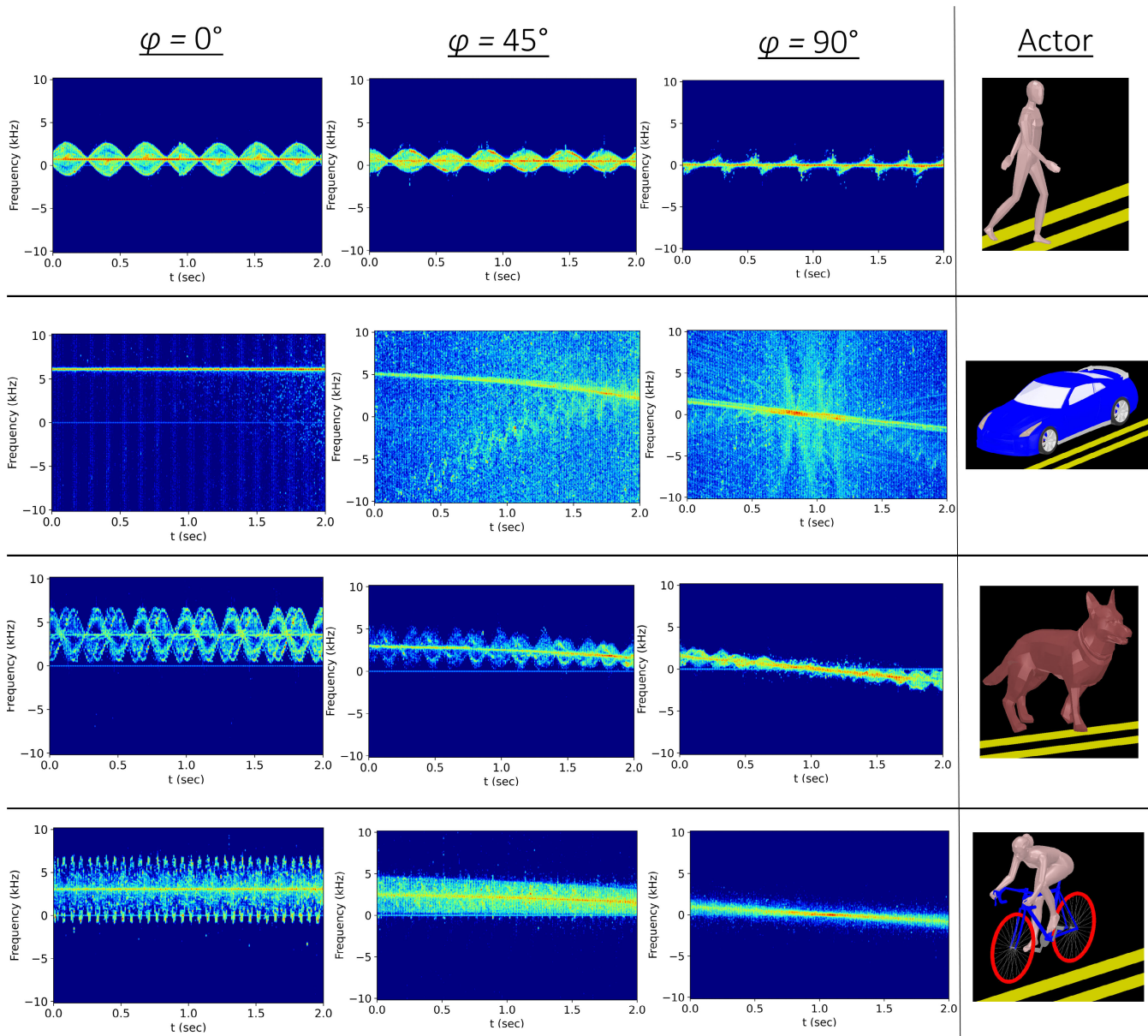
FIGURE 10. Spectrograms for a pedestrian, car, dog and cyclist at three different angles-of-arrival. The spectrogram of each target depends on the angle-of-arrival relative to a stationary radar sensor as shown in Fig. 6.

Another important thing to note is that the bulk Doppler frequency shift, the maxima and minima of the sinusoidal profiles decrease as the angle-of-arrival (AoA) increases from $\phi = 0°$ to $\phi = 90°$. Using (1) it is observed that the overall Doppler frequency shift, f_d, decreases as the AoA, ϕ increases. It is also observed that as the AoA increases from $\phi = 0°$ to $\phi = 90°$, the spectrogram profiles change their shape from sinusoidal to triangular. This change in profile can be attributed to two factors. First, the radar sensor only measures the radial velocity component of the pedestrian's limbs and torso. Second, the human body does not have rotational symmetry. This leads to changes in the Doppler and micro-Doppler responses of the pedestrian as

the AoA changes. Results from this simulation confirm that the spectrogram of a walking pedestrian changes as their AoA changes. Furthermore, the amplitude of micro-Doppler response detected depends on the AoA as well. A possible practical implication of this behavior is that, for two pedestrians at the same range, it may be easier for a radar sensor to accurately classify the pedestrian walking towards the vehicle on a sidewalk ($\phi \approx 0°$) than the pedestrian crossing the road ($\phi \approx 90°$).

C. CAR
A car can be decomposed into its main body and the wheels. The bulk translation of the car is attributed to its body.
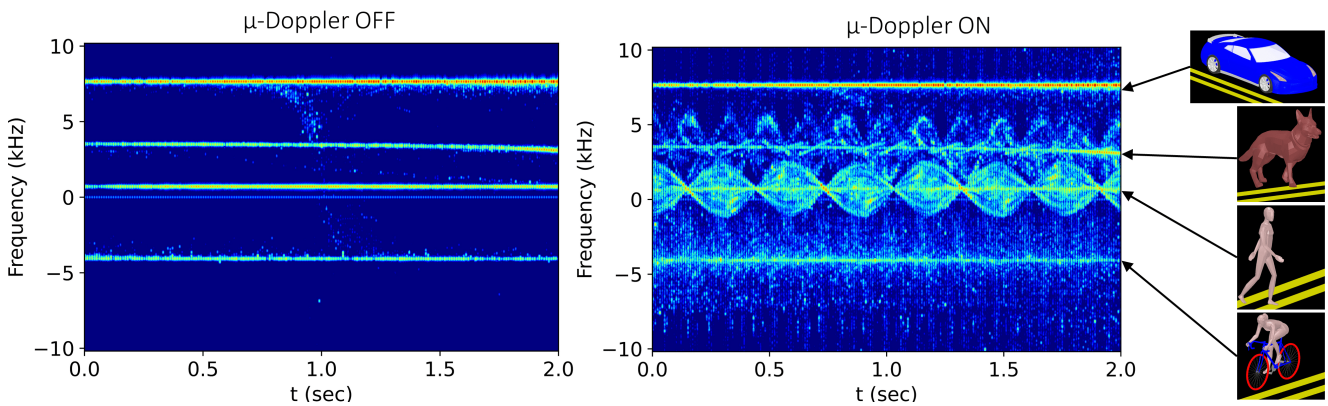
FIGURE 11. Spectrograms of a dog, pedestrian, car and cyclist in the same traffic scene approaching the radar sensor at an angle of arrival of $\phi = 0°$ (see Fig. 6). The simulations are conducted with and without micro-Doppler.

The rotational micro-motion of the wheels are responsible for the micro-Doppler. Fig. 10 shows the spectrograms of a car moving at 12 m/s (approximately 26 mph) observed over 3 different angles-of-arrival (see Fig. 6). Using (1), this corresponds to a Doppler frequency of 6.120 kHz. Fig. 10 shows that a vehicle directly approaching a radar sensor ($\phi = 0°$) does not exhibit pronounced micro-Doppler features. However, rotating the vehicle ($\phi = 45°$ & $\phi = 90°$) exposes the sides of the wheels that typically have metallic rims as shown in Fig. 2 (see Fig. 6). The sides profile of wheel rims can present themselves as electromagnetic scatterers especially at higher frequencies like 77 GHz where the wavelength is 3.8 mm. Therefore, at 77 GHz, seemingly small structural details on the rotating wheels can lead to a strong micro-Doppler response. This behavior was observed in measurements that were conducted in [47] as shown in Fig. 8.

D. DOG
The bulk translation of a running, four legged animal like a dog can be attributed to its upper body. The oscillatory micro-motions (responsible for micro-Doppler) are attributed to the swinging front and back legs. Fig. 10 shows the spectrograms of a dog running at a speed of 7 m/s. The spectrogram of the dog is similar to that of a pedestrian, exhibiting the same sinusoidal profile. However, the spectrogram of a dog shows 4 distinct curves. These curves are in groups of 2 that are approximately 180° out of phase. These groups represent the front and hind pairs of legs. Within each group of curves are 2 additional curves that are slightly out of phase, with each curve representing a specific limb. The spectrogram shown here in Fig. 10 is also an approximation due to the assumed phase-offset, sinusoidal kinematics. The accuracy of this spectrogram can be improved by using MOCAP data or more realistic animations. We do however remark how important details of a running dog's gait cycle can be described by its spectrogram as shown here. Of even greater significance is how simulation can be used to obtain data that would be otherwise impossible or impractical to collect using field measurements. Specifically, it may be futile to try

and dictate the movements of an animal in the manner done in simulations. Using simulation, it is possible to accurately specify the angle-of-arrival, gait, velocity and size of the animal under observation.

E. CYCLIST
A pedaling cyclist can be viewed as a target with a bulk translation associated with the bicycle frame, torso and arms of the cyclist. In addition to this bulk translation, there is additional rotational micro-motion due to the pedaling legs, rotating wheels and pedals. Fig. 10 shows the spectrograms obtained from a cyclist moving at a speed of 6 m/s. Here, sinusoidal profiles belonging to the pedaling legs can be observed. Above these profiles is a series of periodic 'flashes' belonging to the pedals. It has been observed that the micro-Doppler of the wheels and their spokes is much less pronounced when compared to that of the pedaling legs and pedals [27]. This should be compared to car wheels that have a stronger micro-Doppler response due to their larger size and subsequently higher radar cross section (RCS).

F. DISCUSSION
This study showed that each of the targets exhibit unique micro-Doppler behavior. It was also observed that for a single target, its spectrogram strongly depends on its angle-of-arrival relative to the radar sensor. It is important to note that the differences between the spectrograms of each target class were retained regardless of the AoA under consideration. To demonstrate the differences in the spectrograms, a dog, pedestrian, cyclist and car were placed in the same traffic scene. In this simulation, all the actors approached or moved away from the radar sensor at an angle of $\phi = 0°$ (see Fig. 6). Specifically, the dog, pedestrian and car moved towards the stationary radar sensor at speeds of 7 m/s, 1.4 m/s and 15 m/s, respectively. The cyclist was moving away from the radar sensor at a velocity of 8 m/s. Two simulations were run.

In the first case, the motion of the actors was restricted to effectively eliminate micro-Doppler effects. Here, the actors
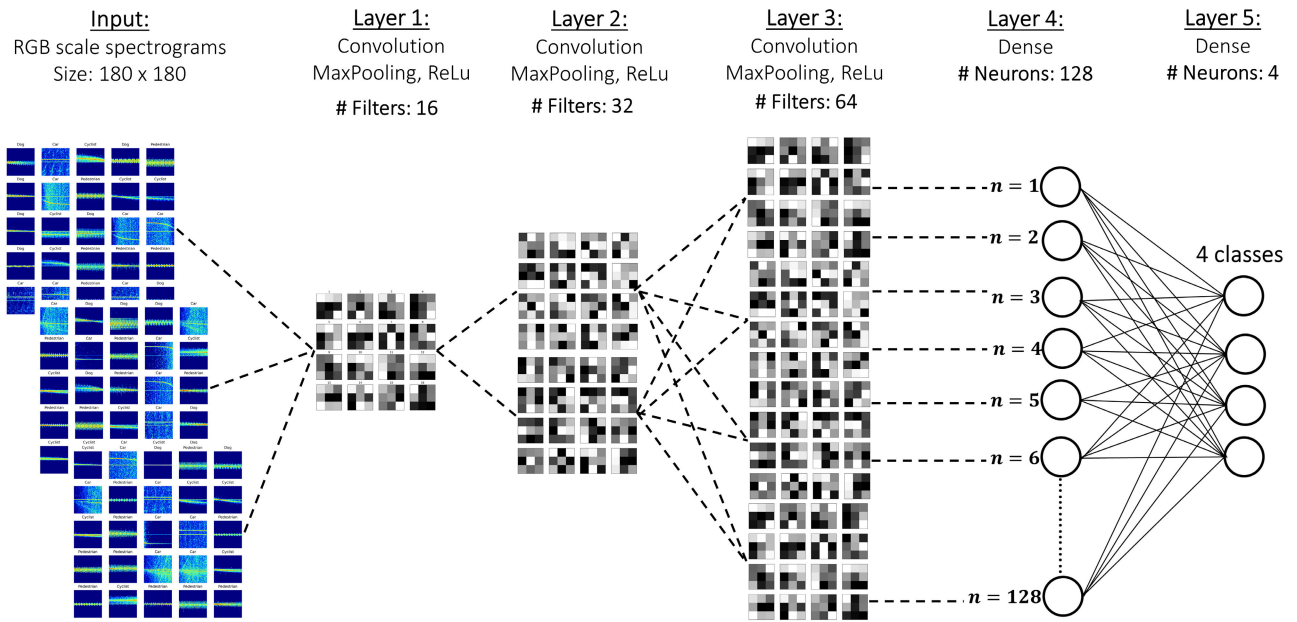
FIGURE 12. A 5-layer Convolutional Neural Network for VRU classification. Each of the filters in the first 3 layers is 3 × 3 in size with a stride of (1,1).
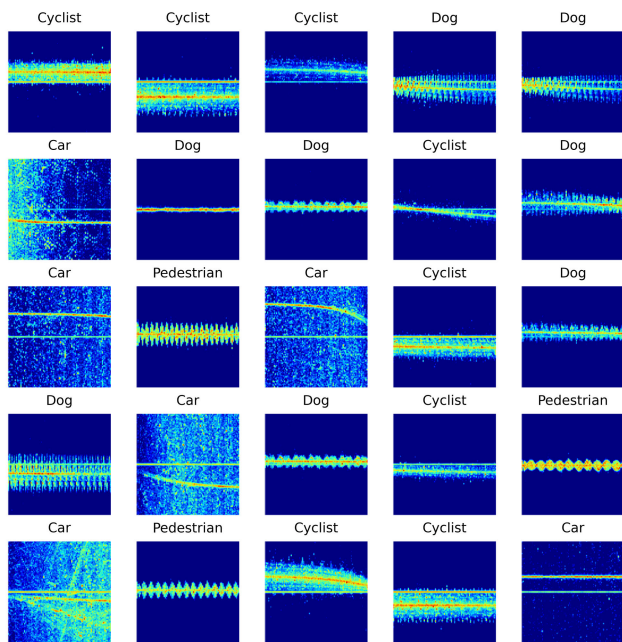

FIGURE 13. Sample of spectrograms used to train a VRU classification Convolutional Neural Network (CNN). The spectrograms were obtained via simulation of 4 typical road users (pedestrian, dog, cyclist and car) with varying angles of arrival and velocity relative to a stationary radar sensor.

FIGURE 14. Visualization of the 16 filters of size 3 × 3 from Layer 1.

still retained their bulk translational velocity while all the micro-motion rotation and oscillation were turned off. Specifically, the dog, cyclist and pedestrian's limbs do not swing when micro-Doppler is turned off. The car and bicycle wheels did not rotate as well. In the second simulation, all the normal micro-Doppler features were turned on. When micro-Doppler is turned off, the actors in the scene are executing motion
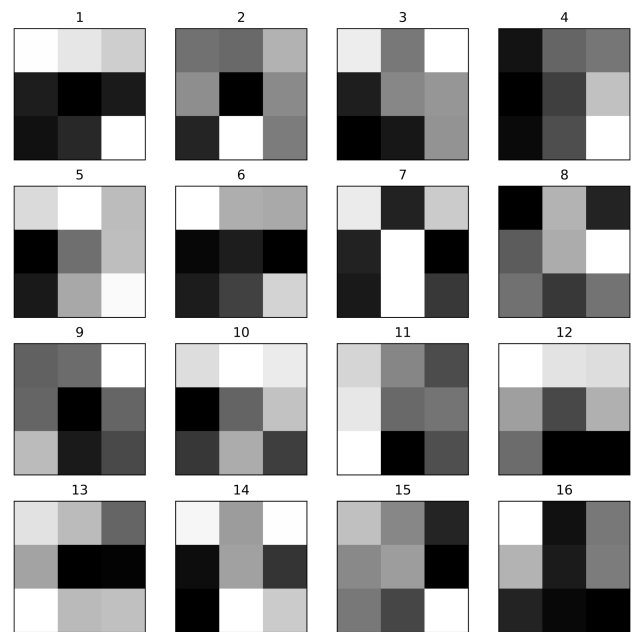
that would not be observed in practice. However, this is a key advantage of simulation as it allows the investigation of cases that are otherwise physically impossible to observe or measure. While such cases can be impractical, they do provide deep insight into the phenomenon under investigation. Fig. 11 shows the spectrograms obtained from these two simulations. Without micro-Doppler information, we observe that each of these actors are much harder to distinguish. Upon re-introducing micro-Doppler, the distinct
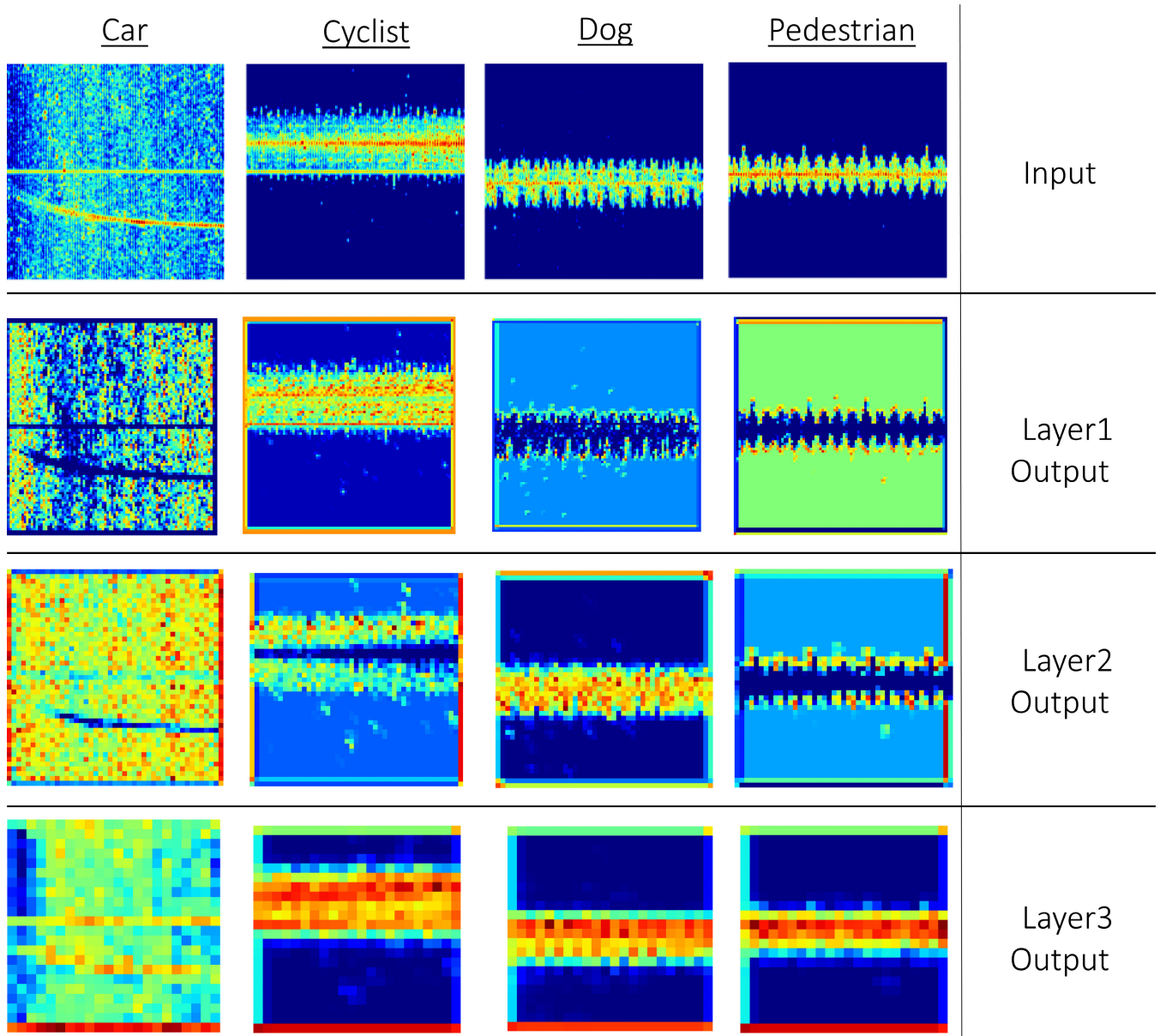
FIGURE 15. Visualization of some samples of feature maps extracted from the 3 convolutional layers after maxpooling.

micro-Doppler signatures can now be observed in the spectrogram. This is the basis for the spectrogram-based VRU classification that will be done using a convolutional neural network in the next section.

V. CONVOLUTIONAL NEURAL NETWORK FOR VRU CLASSIFICATION

Radar signal based classification of VRUs has been achieved in two ways; conventional machine learning (ML) and deep learning (DL). In the conventional ML approach, manual feature extraction is conducted on the radar signals at specific points in the signal processing chain. These features are then used to train classifiers such as the support vector machine

(SVM) [31]–[34]. In [31] classification between pedestrians and static objects was achieved by using the radial velocity variance of each target. Specifically, moving pedestrians exhibited a higher velocity variance than static objects.

The key drawback of traditional ML algorithms is that they depend on manual and usually heuristic feature extraction that requires experience and deep domain knowledge. Furthermore, these classifiers are difficult to generalize and suffer in accuracy when presented with completely new data [32]. On the other hand, deep learning algorithms are capable of automatically extracting these high-level features using a hierarchical architecture [32]. This advantage removes the need for deep domain knowledge. Furthermore,
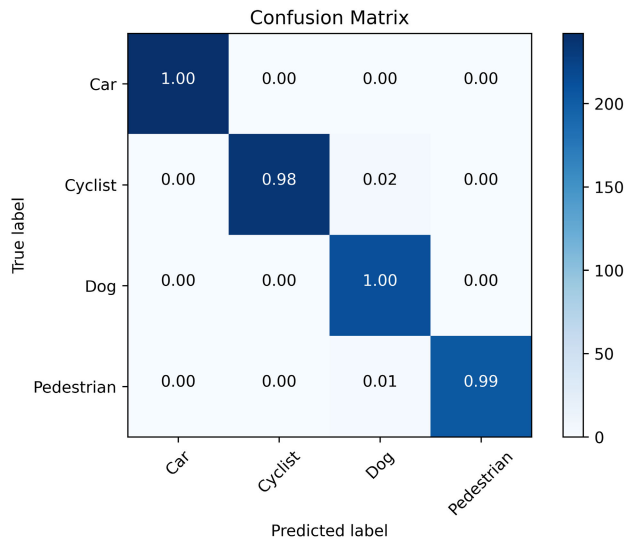
FIGURE 16. Confusion matrix obtained from the CNN shown in Fig. 12 after 5 epochs.

FIGURE 17. CNN classification accuracy over 30 epochs for different data set sizes. *DR* = 1 corresponds to 4,520 samples while *DR* = 0.1 corresponds to 452 total samples used. A 20% validation split was used here.
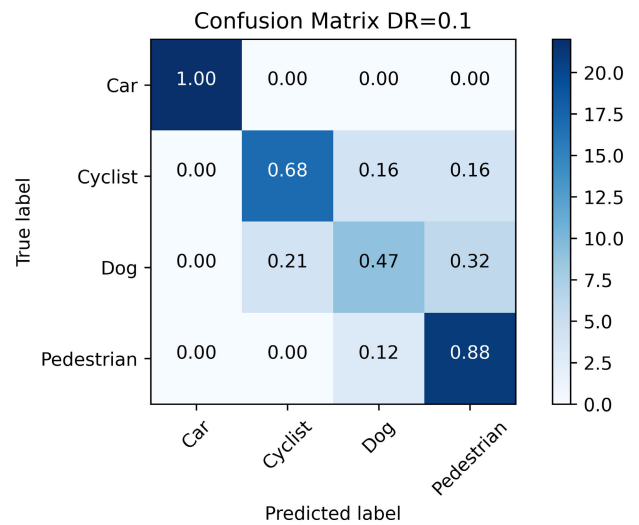

FIGURE 18. Confusion matrix obtained from the CNN shown in Fig. 12 after 10 epochs when trained with only 10% (*DR* = 0.1) of the original data set. The confusion matrix in Fig. 16 is for the original data set(*DR* = 1).
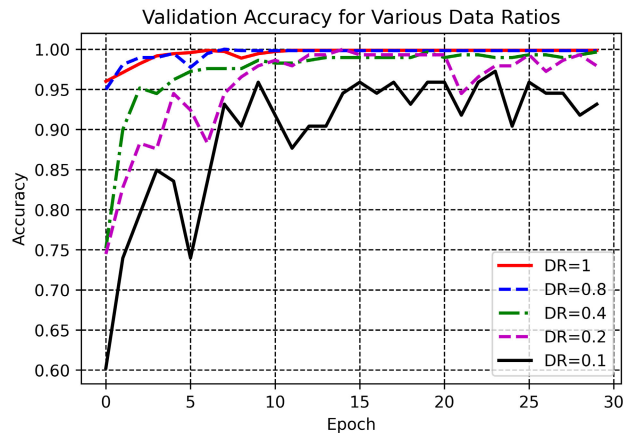
used 16, 32 and 64 filters, respectively. Each filter had a kernel size of 3×3 with a stride of $(1,1)$. Fig. 13 shows a sample of the spectrograms used to train the CNN while Fig. 14 shows 16 filters (single channel) from the first layer. The rectified linear unit function (ReLU) was used as the activation function. The output of the third layer (after max-pooling) was connected to a dense, fully connected layer with 128 neurons. Fig. 15 shows a sample of the extracted feature maps from the 3 convolutional layers after conducting maxpooling.

B. DATA COLLECTION

Before a CNN can reliably classify images, it needs to be trained using a large data set of images that have labels describing the particular class of each image. Fig. 13 shows a sample of 25 spectrograms belonging to the actors shown in Fig. 2. A total of 4,520 spectrograms, equally distributed over the dog, pedestrian, car and cyclist classes were obtained via simulation. For each target class, variation was achieved by changing the velocity and angle-of-arrival (AoA) of each target (see Fig. 6). For specific orientation and velocity values, high fidelity physics-based simulations were conducted over a 2 s time window broken down into discrete 0.01 s time steps. Therefore, a single spectrogram was obtained by simulating 201 coherent processing intervals (CPI). Short time Fourier transform (STFT) analysis using the NumPy library in Python was conducted on synthetic radar signals obtained from the HFSS SBR+ simulations. Ansys OptiSLang [74] was used to automate the parametric velocity/AoA variation, STFT post-processing and file management. Specifically, for each actor, a set of pre-defined AoA and velocity values were passed on to OptiSLang. For example, the average walking speed of a pedestrian is 1.4 m/s. Therefore, the pedestrian was set to approach the stationary the radar sensor at velocities

DL algorithms have easily scalable, automatic feature extraction that makes them robust.

Convolutional neural networks (CNNs) are DL algorithms that are inspired by the visual cortex structure of the eye [29], [32]. Using multiple convolutional layers, CNNs are able to extract higher-level spatial features from lower-level features [32]. Such capabilities make CNNs ideal for image classification and speech recognition. Here, a CNN is used to classify VRUs based on images of their spectrograms. Specifically, using spectrograms, the VRU classification problem can be viewed as an image classification problem.

A. CNN ARCHITECTURE

A 5-layer convolutional neural network (CNN) was used for the image classification [75]. Fig. 12 shows the CNN architecture. This CNN features 3 convolution layers followed by 2 fully connected layers. Layer 1, Layer 2 and Layer 3
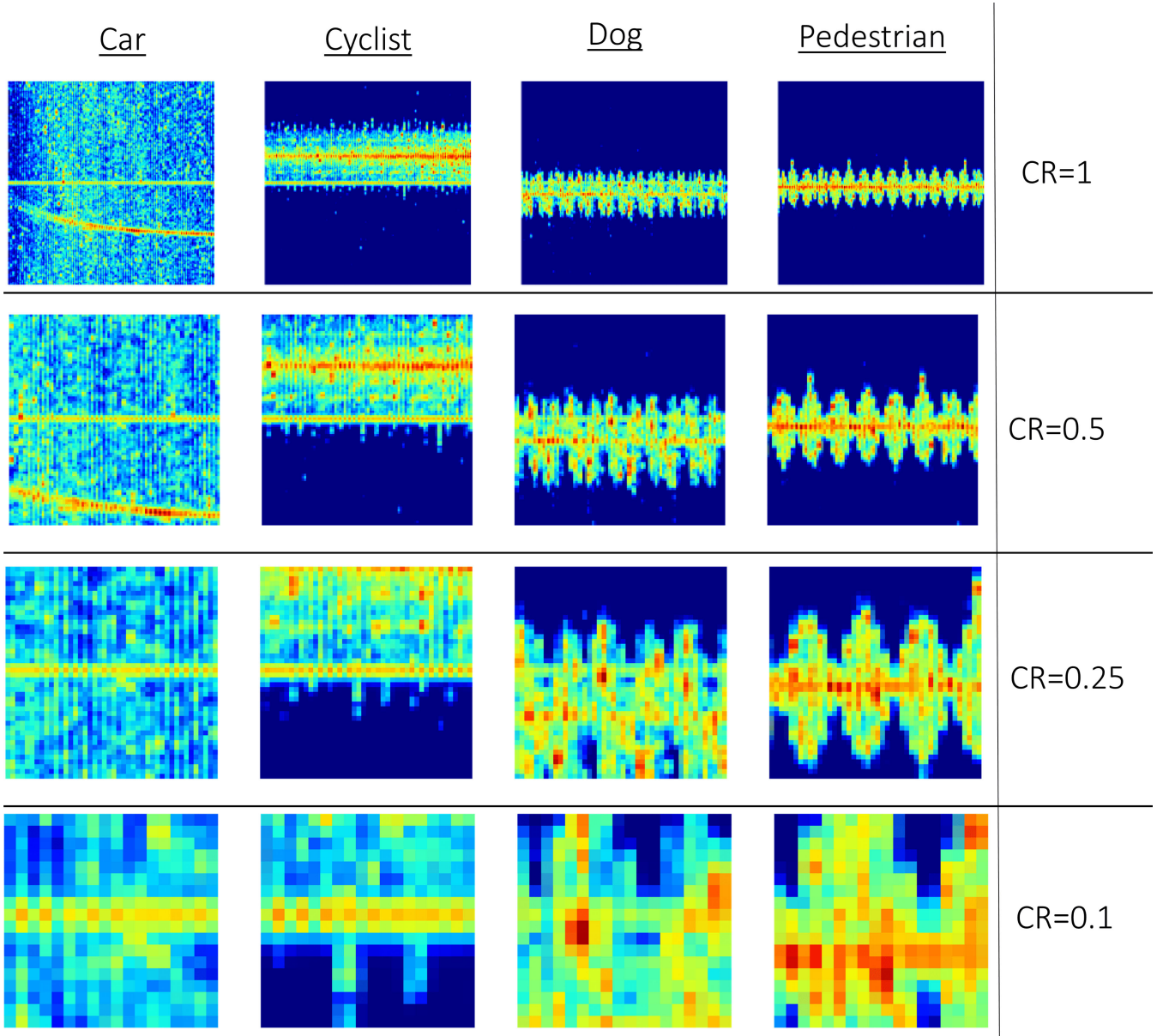
FIGURE 19. Sample data used to train the CNN for different velocity & time observation windows. Velocity/time window augmentation was achieved by cropping the data. *CR* is the cropping ratio. *CR* = 1 corresponds to the original data with an observation window duration of 2 s and max/min velocity of ±20 m/s. *CR* = 0.1 corresponds to an observation window duration of 0.2 s and max/min velocity of ±2 m/s.

of 0.9 m/s, 1.2 m/s, 1.7 m/s, 2 m/s and 2.3 m/s (5 points). The AoA ranged from $\phi = 0°$ to $\phi = 180°$ in increments of 1° (181 points) leading to 905 unique AoA/velocity combinations. For each unique AoA/velocity combination, OptiSLang invoked HFSS SBR+ to simulate the synthetic radar returns required for each spectrogram. After each HFSS SBR+ simulation was completed, post processing was done using the integrated Python environment inside OptiSLang. Finally, a batch script was run inside OptiSLang to save the spectrogram and to delete any result files from the previous simulation. As previously mentioned, it took an average of 90 s to simulate a single spectrogram using a 6 core laptop. It took a total of 4 days and 16 hours to obtain 4,520 spectrograms for this study.

After collecting the data, the Keras application programming interface (API) open-source toolkit was used [76] with the NVIDIA GPU and cuDNN library for acceleration [77]. Using the NVIDIA Quadro® RTX 5000 graphics card and a 6 core, Intel® Core(TM) i7 at 2.6GHz CPU, it took 22.92 s to complete 5 epochs. For any data set size, an initial 20% was removed from the total data and reserved for testing. The CNN was then trained and validated using the remaining data set with a 20% validation split. The confusion matrices shown here were obtained by testing the CNN with the initial, previously unseen 20% test data set. For example, for an initial data set of 4,520 images, 904 images were set aside for testing. This led to a training/validation data set size of 3,616. The CNN was then trained with 80% of the remaining data
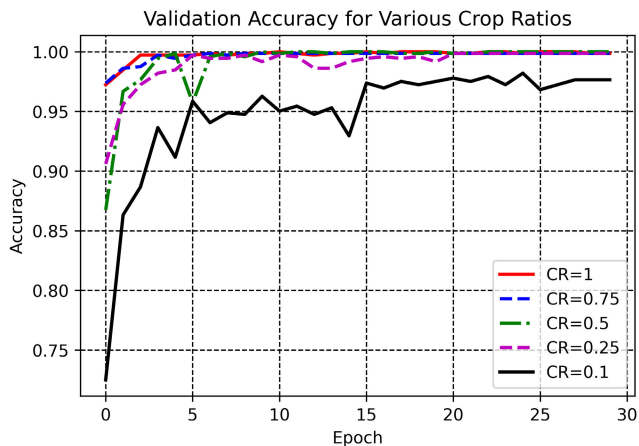
FIGURE 20. CNN classification accuracy over 30 epochs for different observation time windows. Velocity/time window augmentation was achieved by cropping the data. *CR* is the cropping ratio. *CR* = 1 corresponds to the original data with an observation window duration of 2 s and max/min velocity of ±20 m/s. *CR* = 0.1 corresponds to an observation window duration of 0.2 s and max/min velocity of ±2 m/s.
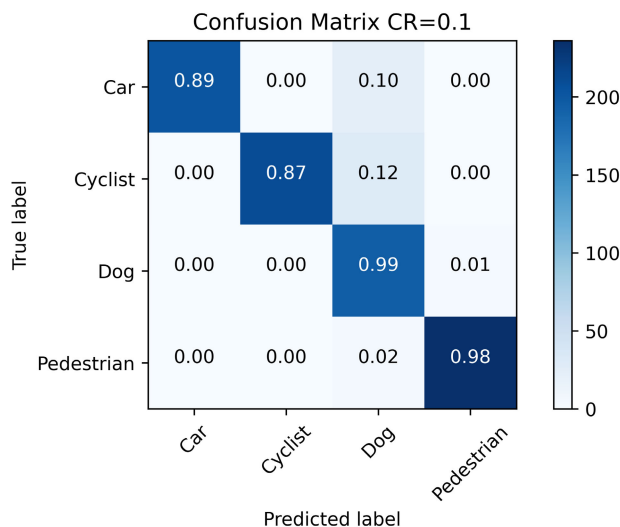

FIGURE 21. Confusion matrix for CNN after 10 epochs with a cropping ratio, *CR* = 0.1. *CR* = 1 corresponds to the original data with an observation window duration of 2 s and max/min velocity window of ±20 m/s (see Fig. 16). *CR* = 0.1 corresponds to an observation window duration of 0.2 s and max/min velocity of ±2 m/s.

set (2,893) and then validated with 20% of the data set (723). The confusion matrix was obtained using the test data (904). Fig. 16 shows the confusion matrix demonstrating a classification accuracy of nearly 100% after 5 epochs.

C. CNN ACCURACY DEPENDENCY ON TRAINING DATA SET SIZE

In addition to the quality and labeling of the data used to train a CNN, the accuracy of a CNN also depends on the data set size used to train it. Specifically, as the data set gets smaller, it becomes harder for the neural network to learn model parameters and achieve generalization. Using generalization, neural networks are able to make better classification predictions on new, previously unseen data and therefore their accuracy improves. Here, we tested the dependence of

the CNN's accuracy on the data set size used to train it. Starting from the initial data set size of 4,520 spectrograms, the size was reduced by multiplying 4,520 by a data-ratio parameter, *DR*. For example, for *DR* = 1, the original data set size was used (4,520 samples) while *DR* values of 0.5 and 0.1 correspond to 2,260 and 452 samples, respectively. A 20% validation split was used in each case. Fig. 17 shows the CNN classification accuracy over 30 epochs for different data set sizes. Fig. 18 shows the confusion matrix for *DR* = 0.1 obtained after 10 epochs. This should be compared to the confusion matrix obtained after only 5 epochs using the original data set (*DR* = 1). As expected, as the data set size gets smaller, the prediction accuracy of the neural network also decreases. It is interesting to note however, that the CNN achieves more than 90% accuracy after 15 epochs with just 10% (*DR* = 0.1) of the original data set.

D. CNN ACCURACY DEPENDENCY ON VELOCITY & TIME OBSERVATION WINDOW AUGMENTATION

The quality of data used to train a CNN can impact its classification accuracy. As the data quality improves, it becomes easier for the neural network to extract the higher-level spatial features from the lower level features in the data. Spectrograms belonging to different VRUs become easier to classify as the time window of observation widens. As the time window gets narrower, higher level features like the periodic, sinusoidal profiles associated with a walking pedestrian can be missed by the CNN (see Fig. 10). The velocity window can also affect spectrogram-based VRU classification. Specifically, reducing the maximum and minimum velocities that can be measured by the radar sensor can lead to velocity ambiguity. Velocity ambiguity was observed to significantly distort the high level features of spectrograms in [27]. A simple way to augment the data quality is to crop the spectrograms. This is akin to making the observation window smaller and reducing the unambiguous minimum and maximum velocities.

The duration of the observation window has practical implications on VRU classification. In highly dynamic traffic scenes, autonomous vehicles will need to detect and classify VRUs with minimum latency. For example, a vehicle travelling at 35 mph (15.64 m/s) will cover a distance of over 30 m in the time it takes to collect data for a 2 s wide spectrogram. Considering the additional time needed from activation of brakes to a complete stop, it is crucial for the VRU classification process to have minimum latency. This can be done by reducing the observation time window duration.

The velocity window also has practical implications on the waveform used for Doppler and micro-Doppler measurement. Specifically, the velocity window is determined by the maximum and minimum velocities that can be unambiguously measured by the radar sensor. Assuming a frequency-modulated continuous-wave (FMCW) radar and symmetrical maximum and minimum velocities, the pulse repetition frequency (PRF) is given by [27]

$$PRF \geq 4V_{\text{max}}/\lambda \qquad (6)$$

Here, V_{max} and λ are the maximum velocity and wavelength at the center frequency. The velocity window is directly proportional to V_{max}. Therefore, the velocity window can be widened by increasing the PRF. It has been observed that for walking pedestrians and a stationary radar sensor, the PRF can be set to 11 kHz without velocity ambiguity [27]. However a radar sensor mounted on a host platform travelling at a speed of 45 mph would require a higher PRF of over 35 kHz to unambiguously determine the Doppler and micro-Doppler of the same pedestrian [27]. This means that a radar sensor with a low PRF may be able to accurately classify a VRU when the host platform is stationary but possibly fail when the platform is in motion. In this work, the radar sensor was assumed to be stationary with a PRF of 20.4 kHz, corresponding to maximum and minimum unambiguous velocities of ± 20 m/s.

Here we tested the dependence of the CNN's classification accuracy on the velocity window and observation window duration. An additional cropping layer was added to the CNN before the first layer shown in Fig. 12. The extent of cropping was represented by the cropping-ratio (CR) variable. Initially, the size of the spectrograms was 180×180, this represents a cropping-ratio of 1(i.e. no cropping). Fig. 19 shows a sample of the data used to train the CNN for different velocity and time windows. The 2-dimensional cropping conducted on the spectrograms can be interpreted as a reduction of the observation window and the waveform PRF (see eqn.6). A cropping-ratio of $CR = 1$ represents an observation window duration of 2 s and maximum and minimum unambiguous velocities of ± 20 m/s (PRF = 20.4 kHz). On the other hand, a cropping-ratio of $CR = 0.1$ represents an observation window duration of 0.2 s and maximum and minimum unambiguous velocities of ± 2 m/s (PRF = 2.04 kHz). As seen in Fig. 19, as CR decreases, it becomes harder for a human to identify the higher-level features that describe representative spectrograms from each class. Fig. 20 shows the CNN classification accuracy over 30 epochs for different observation window duration. Fig. 21 shows the confusion matrix for $CR = 0.1$ obtained after 10 epochs. This should be compared to the confusion matrix obtained after only 5 epochs using the original 2 s observation window duration ($CR = 1$). As expected, as the velocity and observation window gets smaller, the prediction accuracy of the neural network also decreases. It is interesting to note however, that the CNN achieves more than 95% accuracy after 15 epochs with a $0.2s$ observation window. By reducing the observation window duration while maintaining accuracy, autonomous vehicles will be able to classify road actors as VRUs with minimum latency, avoid collisions and possibly save lives.

VI. DISCUSSION: MEASUREMENTS VS. SIMULATION IN ML/AI APPLICATIONS

As previously mentioned, the classification accuracy of a convolutional neural network depends on the quality, quantity and labeling of the data used to train it. In section II, we discussed measurements as a method of obtaining data

for machine learning applications. However cost, time, practicality and repeatability of experiments emerged as key disadvantages. In this paper, we demonstrated a computationally efficient, high-fidelity, physics-based simulation workflow that can be used to obtain large quantities of data for CNN training. However, this workflow is not perfect either. The simulations did not account for system considerations such as receiver sensitivity, noise and other random clutter sources that come in and out of dynamic traffic scene. This led to very 'clean' spectrograms. It is highly likely that a CNN trained using these simulated results would have a diminished classification accuracy when presented with new, noisy data from measurements. Considering the challenges associated with conducting thousands of measurements at 77 GHz [16], [42], [51], it may also be difficult to begin training a CNN with a small and noisy data set. This is the so-called 'cold start' problem. An ideal approach is to strike an optimal balance between the measurement and simulation data sources. For example, experimental data was augmented with simulation data to improve the classification accuracy of a passive WiFi-based healthcare monitoring system in [44]. Here, replacement and augmentation studies were conducted to see the impact of mixing measurement data with simulation data. Results from [44] generally showed that increasing the simulated data in replacement studies led to a drop in the classification accuracy. However, for cases where a small amount of measurement data was available for training, adding simulation data actually improved the classification accuracy by 8%. Therefore, in cases of low volume, noisy and imbalanced measured data, adding simulation data to the CNN training data can actually improve the classification accuracy on new measured data. The goal of this work was to demonstrate a computationally efficient, high-fidelity simulation workflow that can be used to obtain data for initial algorithm development or data augmentation.

VII. CONCLUSION

Radar is one of the enabling sensor technologies in advanced driver assistance systems (ADAS). Vehicles equipped with radar can detect and determine the range, velocity and angle-of-arrival of multiple targets simultaneously. Before they can be deemed safe for the roads, fully autonomous vehicles will need to be able to accurately detect and classify vulnerable road users (VRUs). Further analysis of the reflected radar signal spectrum can be used to classify VRUs by exploiting the micro-Doppler effect. In this paper we used a convolutional neural network (CNN) to classify spectrograms belonging to a pedestrian, car, cyclist and dog. The CNN training data set was obtained using high fidelity physics-based electromagnetic simulations of full scale traffic scenes at 77GHz. A 5-layer CNN was trained using spectrograms obtained from these simulations. The CNN achieved an accuracy of nearly 100% after 5 epochs. Studies were conducted to investigate the impact of training data set size on the classification accuracy of the CNN. Using only 10% of the original data, a classification accuracy of 90% was achieved after

30 epochs. Further studies were conducted to investigate the impact of the velocity window and observation window duration on the classification accuracy of the CNN. Using 10% (0.2 s) of the original velocity/time window, a classification accuracy of over 95% was achieved after 30 epochs. This work showed how high quality, accurately labeled and large data sets for CNN training can be obtained using high fidelity physics-based electromagnetics simulations. Results from this study show that a micro-Doppler based CNN can be used to accurately classify VRUs, help to avoid collisions and ultimately save lives on tomorrow's roads.

ACKNOWLEDGMENT

REFERENCES

[1] R. H. Rasshofer and K. Gresser, "Automotive radar and LiDAR systems for next generation driver assistance functions," *Adv. Radio Sci.*, vol. 3, pp. 205–209, May 2005.

[2] D. M. Gavrila, "The visual analysis of human movement: A survey," *Comput. Vis. Image Understand.*, vol. 73, no. 1, pp. 82–98, Jan. 1999.

[3] T. B. Moeslund, A. Hilton, and V. Krüger, "A survey of advances in vision-based human motion capture and analysis," *Comput. Vis. Image Understand.*, vol. 104, pp. 90–126, Nov./Dec. 2006.

[4] R. Poppe, "Vision-based human motion analysis: An overview," *Comput. Vis. Image Understand.*, vol. 108, nos. 1–2, pp. 4–18, Oct. 2007.

[5] G. Reina, D. Johnson, and J. Underwood, "Radar sensing for intelligent vehicles in urban environments," *Sensors*, vol. 15, no. 6, pp. 14661–14678, Jun. 2015.

[6] J. Hasch, R. Topak, T. Schnabel, T. Zwick, R. Weigel, and C. Waldschmidt, "Millimeter-wave technology for automotive radar sensors in the 77 GHz frequency band," *IEEE Trans. Microw. Theory Techn.*, vol. 60, no. 3, pp. 845–859, Mar. 2012.

[7] K. Ohguchi, M. Shono, and M. Kishida, "79 GHz band ultra-wideband automotive radar," *Fujitsu Ten Tech. J.*, vol. 39, pp. 9–14, Mar. 2013.

[8] J. Singh, S. Rao, and R. Ramasubramanian, "AWR1642 mmWave sensor: 76–81-GHz radar-on-chip for short-range radar applications," Texas Instrum., Dallas, TX, USA, Tech. Rep., 2017, pp. 1–7. [Online]. Available: https://www.ti.com/lit/wp/spyy006/spyy006.pdf

[9] B. H. Ku, P. Schmalenberg, O. Inac, O. D. Gurbuz, J. S. Lee, K. Shiozaki, and G. M. Rebei, "A 77–81 GHz 16 element phased array receiver with ±50° beam scanning for advanced automotive radars," *IEEE Trans. Microw. Theory Techn.*, vol. 62, no. 11, pp. 2823–2831, Nov. 2014.

[10] *Implementing Digital Processing for Automotive Radar Using SoCs*, Altera Corp., San Jose, CA, USA, 2013, pp. 1–15.

[11] O. Toker and S. Alsweiss, "Design of a cyberattack resilient 77 GHz automotive radar sensor," *Electronics*, vol. 9, no. 4, pp. 573–595, Mar. 2020.

[12] NHTSA. (Dec. 2020). *NHTSA Releases 2019 Crash Fatality Data*. [Online]. Available: https://www.nhtsa.gov/press-releases/roadway-fatalities-2019-fars

[13] A. K. Yadav and J. Szpytko, "Safety problems in vehicles with adaptive cruise control system," *J. KONBiN*, vol. 42, no. 1, pp. 389–398, Jun. 2017.

[14] P. Held, D. Steinhauser, A. Kamann, A. Koch, T. Brandmeier, and U. T. Schwarz, "Micro-Doppler extraction of bicycle pedaling movements using automotive radar," in *Proc. IEEE Intell. Vehicles Symp. (IV)*, vol. 35, Jun. 2019, pp. 744–749.

[15] V. C. Chen, F. Li, S.-S. Ho, and H. Wechsler, "Micro-Doppler effect in radar: Phenomenon, model, and simulation study," *IEEE Trans. Aerosp. Electron. Syst.*, vol. 42, no. 1, pp. 2–21, Jan. 2006.

[16] D. Belgiovane and C.-C. Chen, "Micro-Doppler characteristics of pedestrians and bicycles for automotive radar sensors at 77 GHz," in *Proc. 11th Eur. Conf. Antennas Propag. (EUCAP)*, Paris, France, Mar. 2017, pp. 2912–2916.

[17] X. Ma, R. Zhao, X. Liu, H. Kuang, and M. A. Al-Qaness, "Classification of human motions using micro-Doppler radar in the environments with micro-motion interference," *Sensors*, vol. 19, no. 11, pp. 1–19, Jun. 2019.

[18] J. M. Garcia-Rubia, O. Kilic, V. Dang, Q. M. Nguyen, and N. Tran, "Analysis of moving human micro-Doppler signature in forest environments," *Prog. Electromagn. Res.*, vol. 148, pp. 1–14, May 2014. [Online]. Available: http://www.jpier.org/PIER/pier.php?paper=14012306

[19] D. Tahmoush and J. Silvious, "Radar measurement of human polarimetric micro-Doppler," *J. Electr. Comput. Eng.*, vol. 2013, pp. 1–5, Nov. 2013.

[20] S. Abdulatif, F. Aziz, B. Kleiner, and U. Schneider, "Real-time capable micro-Doppler signature decomposition of walking human limbs," in *Proc. IEEE Radar Conf. (RadarConf)*, Seattle, WA, USA, May 2017, pp. 1093–1098.

[21] Y. Kim and T. Moon, "Human detection and activity classification based on micro-Doppler signatures using deep convolutional neural networks," *IEEE Geosci. Remote Sens. Lett.*, vol. 13, no. 1, pp. 8–12, Jan. 2016.

[22] Y. Lang, C. Hou, Y. Yang, D. Huang, and Y. He, "Convolutional neural network for human micro-Doppler classification," in *Proc. Eur. Microw. Conf.*, Nuremberg, Germany, Oct. 2017, pp. 1–4.

[23] A. K. Singh and Y. H. Kim, "Analysis of human kinetics using millimeter-wave micro-Doppler radar," *Procedia Comput. Sci.*, vol. 84, pp. 36–40, Jan. 2016.

[24] S. Z. Gürbüz, B. Tekeli, M. Yüksel, C. Karabacak, A. C. Gürbüz, and M. B. Guldogan, "Importance ranking of features for human micro-Doppler classification with a radar network," in *Proc. 16th Int. Conf. Inf. Fusion*, İstanbul, Turkey, Jul. 2013, pp. 610–616.

[25] S. Bjorklund, H. Petersson, A. Nezirovic, M. B. Guldogan, and F. Gustafsson, "Millimeter-wave radar micro-Doppler signatures of human motion," in *Proc. 12th Int. Radar Symp. (IRS)*, Sep. 2011, pp. 167–174.

[26] M. Stolz, E. Schubert, F. Meinl, M. Kunert, and W. Menzel, "Multi-target reflection point model of cyclists for automotive radar," in *Proc. Eur. Radar Conf. (EURAD)*, Nuremberg, Germany, Oct. 2017, pp. 94–97.

[27] H. Yan, W. Doerr, A. Ioffe, and H. Clasen, "Micro-Doppler based classifying features for automotive radar VRU target classification," in *Proc. 25th Int. Tech. Conf. Enhanced Saf. Vehicles (ESV)*, Detroit, MI, USA, Jun. 2017, pp. 1–8.

[28] S. Rahman and D. A. Robertson, "Radar micro-Doppler signatures of drones and birds at K-band and W-band," *Sci. Rep.*, vol. 8, no. 1, pp. 1–11, Dec. 2018.

[29] Y. Liu and J. Liu, "Recognition and classification of rotorcraft by micro-Doppler signatures using deep learning," in *Proc. Int. Conf. Comput. Sci.*, in Lecture Notes in Computer Science, vol. 10860. Springer, Jun. 2018, pp. 141–152. [Online]. Available: https://link.springer.com/chapter/10.1007/978-3-319-93698-7_11

[30] Y. Li, L. Du, and H. Liu, "Moving vehicle classification based on micro-Doppler signature," in *Proc. IEEE Int. Conf. Signal Process., Commun. Comput. (ICSPCC)*, Xi'an, China, Sep. 2011, pp. 1–4.

[31] A. Bartsch, F. Fitzek, and R. H. Rasshofer, "Pedestrian recognition using automotive radar sensors," *Adv. Radio Sci.*, vol. 10, pp. 45–55, Sep. 2012.

[32] X. Li, Y. He, and X. Jing, "A survey of deep learning-based human activity recognition in radar," *Remote Sens.*, vol. 11, no. 9, pp. 1–22, May 2019.

[33] J. Zabalza, C. Clemente, G. D. Caterina, J. Ren, J. J. Soraghan, and S. Marshall, "Robust PCA micro-Doppler classification using SVM on embedded systems," *IEEE Trans. Aerosp. Electron. Syst.*, vol. 50, no. 3, pp. 2304–2310, Jul. 2014.

[34] Y. Kim and H. Ling, "Human activity classification based on micro-Doppler signatures using a support vector machine," *IEEE Trans. Geosci. Remote Sens.*, vol. 47, no. 5, pp. 1328–1337, May 2009.

[35] M. S. Seyfioglu, B. Erol, S. Z. Gurbuz, and M. G. Amin, "DNN transfer learning from diversified micro-Doppler for motion classification," *IEEE Trans. Aerosp. Electron. Syst.*, vol. 55, no. 5, pp. 2164–2180, Oct. 2019.

[36] D. Yang and L. Zhou, "Use of deep neural networks for classification of micro-Doppler signature from radar data," M.S. thesis, Dept. MPCOM, MPSYS, Chalmers Univ. Technol., Gothenburg, Sweden, 2018.

[37] B. Choi and D. Oh, "Classification of drone type using deep convolutional neural networks based on micro-Doppler simulation," in *Proc. Int. Symp. Antennas Propag. (ISAP)*, Busan, South Korea, 2018, pp. 1–2.

[38] J. Kwon and N. Kwak, "Human detection by neural networks using a low-cost short-range Doppler radar sensor," in *Proc. IEEE Radar Conf. (RadarConf)*, May 2017, pp. 755–760.

[39] M. S. Seyfioglu, S. Z. Gurbuz, A. M. Öbayoglu, and M. Yuksel, "Deep learning of micro-Doppler features for aided and unaided gait recognition," in *Proc. IEEE Radar Conf. (RadarConf)*, May 2017, pp. 1125–1130.

[40] R. Boulic, N. M. Thalmann, and D. Thalmann, "A global human walking model with real-time kinematic personification," *Vis. Comput.*, vol. 6, no. 6, pp. 344–358, Nov. 1990.

[41] P. van Dorp and F. C. A. Groen, "Human walking estimation with radar," *IEE Proc., Radar, Sonar Navigat.*, vol. 150, no. 5, pp. 356–365, Oct. 2003.

[42] D. Belgiovane, C.-C. Chen, M. Chen, S. Y.-P. Chien, and R. Sherony, "77 GHz radar scattering properties of pedestrians," in *Proc. IEEE Radar Conf.*, Cincinnati, OH, USA, May 2014, pp. 735–738.

[43] S. Villeval, I. Bilik, and S. Z. Gurbuz, "Application of a 24 GHz FMCW automotive radar for urban target classification," in *Proc. IEEE Radar Conf.*, Cincinnati, OH, USA, May 2014, pp. 1237–1240.

[44] C. Tang, S. Vishwakarma, W. Li, R. Adve, S. Julier, and K. Chetty, "Augmenting experimental data with simulations to improve activity classification in healthcare monitoring," in *Proc. IEEE Radar Conf. (RadarConf)*, Atlanta, GA, USA, May 2021, pp. 1–6.

[45] D. Belgiovane and C.-C. Chen, "Bicycles and human riders backscattering at 77 GHz for automotive radar," in *Proc. 10th Eur. Conf. Antennas Propag. (EuCAP)*, Davos, Switzerland, Apr. 2016, pp. 1–5.

[46] N. Pandey, G. Duggal, and S. S. Ram, "Database of simulated inverse synthetic aperture radar images for short range automotive radar," in *Proc. IEEE Int. Radar Conf. (RADAR)*, Washington, DC, USA, Apr. 2020, pp. 238–243.

[47] G. Duggal, S. Vishwakarma, K. V. Mishra, and S. S. Ram, "Doppler-resilient 802.11ad-based ultrashort range automotive joint radar-communications system," *IEEE Trans. Aerosp. Electron. Syst.*, vol. 56, no. 5, pp. 4035–4048, Oct. 2020.

[48] S. Lee, Y. Yoon, J. Lee, and S. Kim, "Human–vehicle classification using feature-based SVM in 77-GHz automotive FMCW radar," *IET Radar, Sonar Navigat.*, vol. 11, no. 10, pp. 1589–1596, Oct. 2017.

[49] B. Erol and S. Z. Gurbuz, "A kinect-based human micro-Doppler simulator," *IEEE Aerosp. Electron. Syst. Mag.*, vol. 30, no. 5, pp. 6–17, May 2015.

[50] C. Karabacak, S. Z. Gurbuz, A. C. Gurbuz, M. B. Guldogan, G. Hendeby, and F. Gustafsson, "Knowledge exploitation for human micro-Doppler classification," *IEEE Geosci. Remote Sens. Lett.*, vol. 12, no. 10, pp. 2125–2129, Oct. 2015.

[51] S. B. Jayapal Gowdu, A. Schwind, R. Stephan, and M. A. Hein, "Monostatic RCS measurements of a passenger car mock-up at 77 GHz frequency in virtual environment," in *Proc. 49th Eur. Microw. Conf. (EuMC)*, Paris, France, Oct. 2019, pp. 996–999.

[52] S. S. Ram and H. Ling, "Microdoppler signature simulation of computer animated human and animal motions," in *Proc. IEEE Antennas Propag. Soc. Int. Symp.*, San Diego, CA, USA, Jul. 2008, pp. 1–4.

[53] S. Sundar Ram and H. Ling, "Simulation of human micro Dopplers using computer animation data," in *Proc. IEEE Radar Conf.*, Rome, Italy, May 2008, pp. 1–6.

[54] A. D. Singh, S. S. Ram, and S. Vishwakarma, "Simulation of the radar cross-section of dynamic human motions using virtual reality data and ray tracing," in *Proc. IEEE Radar Conf. (RadarConf)*, Oklahoma City, OK, USA, Apr. 2018, pp. 1555–1560.

[55] The Ohio State University. *Advanced Computer Center for the Arts and Design (ACCAD): Motion Lab*. Accessed: Jun. 4, 2021. [Online]. Available: https://accad.osu.edu/research/motion-lab

[56] Carnegie Mellon University. *CMU Graphics Lab Motion Capture Database*. Accessed: Jun. 4, 2021. [Online]. Available: http://mocap.cs.cmu.edu/

[57] H. Chen, R. Gentile, C. Wang, and S. James. (Jan. 2020). Algorithms to antenna: Classifying radar micro-Doppler signatures. Microwave RF. [Online]. Available: https://www.mwrf.com/technologies/systems/article/21120548/algorithms-to-antenna-classifying-radar-microdoppler-signatures

[58] *HFSS SBR+ Technical Overview, 2020 R1 Online Help*, Ansys Electron., Canonsburg, PA, USA, 2020.

[59] A. P. Sligar, "Machine learning-based radar perception for autonomous vehicles using full physics simulation," *IEEE Access*, vol. 8, pp. 51470–51476, 2020.

[60] R. A. Kipp, "Curved surface scattering geometry in the shooting and bouncing rays method," in *Proc. IEEE Antennas Propag. Soc. Int. Symp.*, Toronto, ON, Canada, Jul. 2010, pp. 1–4.

[61] U. Chipengo, P. M. Krenz, and S. Carpenter, "From antenna design to high fidelity, full physics automotive radar sensor corner case simulation," *Model. Simul. Eng.*, vol. 2018, pp. 1–19, Dec. 2018.

[62] U. Chipengo, A. Sligar, and S. Carpenter, "High fidelity physics simulation of 128 channel MIMO sensor for 77 GHz automotive radar," *IEEE Access*, vol. 8, pp. 160643–160652, 2020.

[63] U. Chipengo and M. Commens, "A 77 GHz simulation study of roadway infrastructure radar signatures for smart roads," in *Proc. 16th Eur. Radar Conf. (EuRAD)*, Paris, France, 2019, pp. 137–140.

[64] J. D. Castro, S. Singh, A. Arora, S. Louie, and D. Senic, "Enabling safe autonomous vehicles by advanced mm-wave radar simulations," in *IEEE MTT-S Int. Microw. Symp. Dig.*, Boston, MA, USA, Jun. 2019, pp. 1476–1479.

[65] REMCOM. *Near Field Propagation Method in Automotive Radar Simulations*. Accessed: Jun. 4, 2021. [Online]. Available: https://www.remcom.com/wavefarer-nearfield-propagation-method

[66] AFRL DSRC. *XPATCH, High Performance Software*. Accessed: Jun. 4, 2021. [Online]. Available: https://www.afrl.hpc.mil/software/description.html?app=xpatch

[67] Ansys. *Ansys HFSS: Best-in-Class 3D High Frequency Electromagnetic Simulation Software*. Accessed: Jun. 4, 2021. [Online]. Available: https://www.ansys.com/products/electronics/ansys-hfss

[68] A. Elfrgani and C. J. Reddy, "Near-field RCS for automotive radar applications," in *Proc. Int. Workshop Antenna Technol. (iWAT)*, Miami, FL, USA, Mar. 2019, pp. 217–220.

[69] S. M. Patole, M. Torlak, D. Wang, and M. Ali, "Automotive radars: A review of signal processing techniques," *IEEE Signal Process. Mag.*, vol. 34, no. 2, pp. 22–35, Mar. 2017.

[70] J. Li and P. Stoica, "MIMO radar with colocated antennas," *IEEE Signal Process. Mag.*, vol. 24, no. 5, pp. 106–114, Sep. 2007.

[71] Z. Zhang, C. Zhou, Y. Gu, and Z. Shi, "FFT-based DOA estimation for coprime MIMO radar: A hardware-friendly approach," in *Proc. IEEE 23rd Int. Conf. Digit. Signal Process. (DSP)*, Shanghai, China, Nov. 2018, pp. 1–5.

[72] E. Fishler, A. Haimovich, R. Blum, D. Chizhik, L. Cimini, and R. Valenzuela, "MIMO radar: An idea whose time has come," in *Proc. IEEE Radar Conf.*, Philadelphia, PA, USA, Apr. 2004, pp. 71–78.

[73] S. Lutz, K. Baur, and T. Walter, "77 GHz lens-based multistatic MIMO radar with colocated antennas for automotive applications," in *IEEE MTT-S Int. Microw. Symp. Dig.*, Montreal, QC, Canada, Jun. 2012, pp. 1–3.

[74] Ansys. *Ansys optiSLang: Process Integration & Robust Design Optimization*. Accessed: Jun. 4, 2021. [Online]. Available: https://www.ansys.com/products/platform/ansys-optislang

[75] TensorFlow. *Image Classification*. Accessed: Jun. 4, 2021. [Online]. Available: https://www.tensorflow.org/tutorials/images/classification

[76] Keras. *Keras: Simple, Flexible, Powerful*. Accessed: Jun. 4, 2021. [Online]. Available: https://keras.io

[77] NVIDIA. *NVIDIA Transfer Learning Toolkit*. Accessed: Jun. 4, 2021. [Online]. Available: https://developer.nvidia.com/CUDnn

[78] Q. Yi, S. Chien, L. Li, W. Niu, Y. Chen, D. Good, C.-C. Chen, and R. Sherony, "Development of test scenarios and bicyclist surrogate for the evaluation of bicyclist automatic emergency braking systems," *J. Intell. Connected Vehicles*, vol. 1, no. 1, pp. 15–27, Oct. 2018.

[79] Math Works. *Back-Scatter Radar Signals From Bicyclist, MathWorks Help Center*. Accessed: Jun. 4, 2021. [Online]. Available: https://www.mathworks.com/help/radar/ref/backscatterbicyclist.html

[80] S. Pradeepth and K. P. Peeyush, "Vehicle wheel detection using micro Doppler effect," *J. Phys., Conf. Ser.*, vol. 1706, pp. 1–7, Aug. 2020.

[81] Math Works. *Pedestrian and Bicyclist Classification Using Deep Learning, MathWorks Help Center*. Accessed: Jun. 4, 2021. [Online]. Available: https://www.mathworks.com/help/radar/ug/pedestrian-and-bicyclist-classification-using-deep-learning.html

USHEMADZORO CHIPENGO received the B.S. degree in electrical engineering from the University of Nicosia, Cyprus, in 2013, and the M.Sc. and Ph.D. degrees in electrical engineering from The Ohio State University, in 2017, with a focus on electromagnetics, he has conducted research on slow wave structures for high power microwave sources, antennas, microwave circuits, and computational electromagnetics.

In 2017, he joined Ansys Inc., where he is currently a Senior Application Engineer. He uses his expertise in simulation to solve a wide range of electromagnetics problems. His current research interests include slow wave structures for high power microwave sources, antenna design for automotive applications (V2V, V2I, 5G, RKE, and satellite radio), and automotive radar for advanced driver assistance systems (ADAS).

ARIEN P. SLIGAR received the B.S. and M.Sc. degrees in electrical engineering from Oregon State University, in 2004 and 2006, respectively, with a focus on electromagnetics and microwave components.

In 2006, he joined Ansys Inc., where he is currently a Principal Engineer with a focus on advanced applications of numerical simulation for electromagnetics and electronics. He is an expert in the application of electromagnetic field simulation to the design of antennas, complex antenna systems, microwave components, and high-speed electronics. He works with leading technology companies and provides engineering guidance allowing them to successfully apply simulation and automated workflows to their most difficult design challenges.

STEFANO MIHAI CANTA received the Laurea and Laurea Magistrale degrees in telecommunications engineering from the Politecnico di Milano, in 2003 and 2006, respectively, and the M.Sc. and Ph.D. degrees in electrical and computer engineering from the University of Illinois at Chicago, in 2009 and 2010, respectively.

In 2010, he joined SSL, now Maxar, as an Antenna Engineering Specialist. He joined Ansys Inc., in 2015, during the acquisition of Delcross Technologies, where he is currently a Lead Research and Development Engineer with the HFSS SBR+ Asymptotics Group. His research interests include SBR+ performance and accuracy with creeping waves, automotive radar simulations, radar signal processing, and reflector antenna analysis.

MARKUS GOLDGRUBER received the B.Sc., M.Sc., and Ph.D. degrees in civil engineering from the Graz University of Technology, in 2009, 2011, and 2015, respectively, with a focus on structural analysis with the finite elements method.

He has conducted research on nonlinear seismic simulations on large concrete arch dams, to study the impact of seismic events onto these structures in detail. He joined Ansys Inc., during the 2019 acquisition of Dynardo, where he was working for approximately four years. He is currently the Application Engineering Manager of the Ansys OptiSLang Product. In the last years, he was responsible for several projects worldwide in the field of variational analysis, process automation and design optimization to help customers automating their simulation processes, improve products, and generating sophisticated metamodels from 0D to 3D, to be used digital twins.

HEN LEIBOVICH received the B.Sc. degree in electrical engineering from the Jerusalem College of Engineering, Israel, in 2011, with a focus on communication and electromagnetics.

In 2016, he joined Ansys Inc., where he is currently an Application Engineer, with a focus on aerospace and defense microwave applications, antenna design for autonomous application, and consumer electronics. He supports companies in wide range of RF and microwave applications to successfully apply simulations in their design process.

SHAWN CARPENTER received the B.E.E. degree in electrical engineering from the University of Minnesota Institute of Technology, in 1988, and the M.S.E.E. degree in electrical engineering from Syracuse University, in 1991, concurrently with the General Electric Thomas Edison Advanced Course in Engineering Program.

He has served as a Senior Microwave Engineer in module design and array technology with the GE Aerospace Electronics Laboratory, Syracuse, NY, USA; the VP of Sales and Marketing with Sonnet Software Inc., and the Director and a Sales and Marketing Executive with Delcross Technologies. He joined Ansys Inc., during the 2015 acquisition of Delcross Technologies. He is currently the Senior Product Manager of the Ansys Electronic Business Unit and the Program Director of 5G. His current research interests include phased array modeling techniques for MIMO and adaptive beamforming, installed antenna-host interactions, and mm-wave radar sensor modeling and physical channel modeling for electrically large environments.

● ● ●